Genetic relationship between hydrocarbon system evolution and Carlin-type gold mineralization: Insights from Re-Os pyrobitumen and pyrite geochronology in the Nanpanjiang Basin, South China

Xiang Ge[1], David Selby[2,3], Junjie Liu[2,4], Youzhi Chen[5], Guofan Cheng[5], Chuanbo Shen[1*]

[1] Key Laboratory of Tectonics and Petroleum Resources, China University of Geosciences, Ministry of Education, Wuhan, 430074, China

[2] Department of Earth Sciences, Durham University, Durham DH1 3LE, UK

[3] State Key Laboratory of Geological Processes and Mineral Resources, China University of Geosciences, Wuhan 430074, China

[4]State Key Laboratory of Isotope Geochemistry, Guangzhou Institute of Geochemistry, Chinese Academy of Sciences, Guangzhou, 510640, China

[5] School of Resources and Environmental Engineering，Guizhou Institute of Technology，Guiyang 550003, China

Corresponding Author:

Professor Dr. Chuanbo Shen (Shen, C.B.)

Postal address: Key Laboratory of Tectonics and Petroleum Resources, China University of Geosciences, Ministry of Education, Wuhan, 430074, China

E-mail: cbshen@cug.edu.cn, cugshen@126.com

Tel.: +86-27-67883067; Fax. +86-27-67883051

ABSTRACT

The spatial association of hydrocarbons with metalliferous ore deposits is found worldwide and is particularly common to Carlin-type gold systems. Both liquid oil and pyrobitumen are found in Carlin-type gold deposits of North Nevada, USA and the Nanpanjiang Basin, South China. However, the temporal and genetic association of hydrocarbons and gold mineralization are still debated. To this end, using rhenium-osmium (Re-Os) geochronology of pyrobitumen and gold-bearing pyrite from the Laizishan and Banqi reservoirs and the Yata Carlin-type gold deposit in the Nanpanjiang Basin, we consider hydrocarbons played a critical role in the mineralization process.

A Re-Os age of 228 ± 16 Ma obtained for highly mature pyrobitumen suggests that liquid oil cracking occurred during the Late Triassic in the Laizishan and Banqi reservoirs. This age is in agreement with the modelled thermal history of the Nanpanjiang Basin. Additionally, a broadly identical gold-bearing pyrite Re-Os age of 218 ± 25 Ma from Yata Carlin-type gold deposit which is in agreement with ages reported for other Carlin-type gold deposits in the Nanpanjiang Basin (e.g., in-situ SIMS U-Pb rutile = 213.6 ± 5.4 Ma, Re-Os arsenopyrite = 204 ± 19 Ma - 235 ± 33 Ma and Rb-Sr illite = 212.8 ± 4.6 Ma) suggests the auriferous Carlin-type systems of the Nanpanjiang Basin also formed during the Late Triassic. Integrating our Re-Os data, with recent liquid hydrocarbon experimental data and fluid inclusion data from both reservoirs and gold deposits within the Nanpanjiang Basin, a methane (CH_4) dominated thermochemical sulfate reduction (TSR) process, which introduced

hydrogen sulfide (H_2S) into basinal fluid and ultimately led to the deposition of gold-bearing pyrite by sulfidation, is considered to be the genetic link between of pyrobitumen and gold-bearing pyrite mineralization of the Carlin-type systems of the Nanpanjiang Basin.

Key words:

Re-Os geochronology; pyrobitumen; pyrite; Carlin-type gold deposit; Nanpanjiang Basin; South China

1. INTRODUCTION

Sedimentary basins host key source units for both hydrocarbon and metal resources (Parnell, 1994; Liu et al., 2000). In many cases, both a temporal and spatial relationship exists between hydrocarbon migration/accumulation and the formation of mineral systems, such as Mississippi Valley-type (MVT) lead-zinc deposits in the Midcontinent, USA, and Nunavut, Canada (Anderson, 1975; Kesler et al., 1994; Selby et al., 2005; Saintilan et al., 2019), sandstone uranium deposits in the ChuSarysu and Syrdarya basins in Kazakhstan (Jaireth et al., 2008), and vein-type uranium deposits in Czech Republic (Kribek et al., 1999). Hydrocarbons (oil, bitumen or pyrobitumen) are also associated with gold systems worldwide, for example gold-uranium deposits in the Witwatersrand Basin, South Africa (Robb and Meyer, 1995; Fuchs et al., 2016), the Owen Lake epithermal Ag-Au vein deposit, central British Columbia (Thomson et al., 1992), orogenic gold deposits both in Cosmo Howley, Northern territories,

Australia and West Qinling, China (Mirasol-Robert et al., 2017; Xiong et al., 2019; Wu et al., 2020) and Carlin-type gold deposits in the Alligator Ridge district, Nevada, USA (Hulen et al., 1998; Hulen and Collister, 1999; Muntean, 2018a). Carlin-type gold deposits (micro-disseminated gold commonly hosted in hydrothermal pyrite ± arsenopyrite) are a hydrothermal deposit type occurring in certain types of sedimentary basins (Hofstra and Cline, 2000). Differences between the Carlin-style deposits in Nevada and other similar deposits worldwide have led to a proliferation of terms, including Carlin-type, Carlin-like, sedimentary rock-hosted and distal disseminated, gold deposits. Characteristics including tectonic setting, host rocks, gold occurrence, hydrothermal alteration, and ore paragenesis were used to define those types of gold deposits (Muntean, 2018b). Comparison of the gold deposits in Nevada and the Nanpanjiang Basin, South China, show that both groups of deposits have, (1) a similar tectonic evolution; (2) invisible gold residing in fine-grained (<10 μm) pyrite or within pyrite rims on gold-poor pyrite cores (Su et al., 2012; Cline, 2018; Yan et al., 2018); (3) host rocks consisting of limestone and/or calcareous siltstone; and (4) alteration assemblages that reflect sulfidation, decarbonatization, silicification, and argillization processes (Xie et al., 2018a). These similarities, notwithstanding some differences including ore-stage pyrite morphology, wall rock alteration, CO_2 abundance in the ore fluids (Xie et al., 2018a), suggest that the gold deposits in the Nanpanjiang Basin belong to the Carlin-type classification (Muntean, 2018b). The Carlin-type gold deposits of the Nanpanjiang Basin, with an estimated

89 reserve of more than 700 tonnes of Au, make the region the second largest in the
90 world after Nevada (Jin et al., 2016; Muntean, 2018a; Su et al., 2018).

91 Similar to the Carlin-type gold deposits in Alligator Ridge district, Nevada (Hulen
92 and Collister, 1999; Nutt and Hofstra, 2003), hydrocarbon, especially pyrobitumen, is
93 spatially related to the gold deposits in the Nanpanjiang Basin (Gu et al., 2010; Tan et
94 al., 2015; Liu et al., 2016) (Fig. 1). However, any role of hydrocarbons in the formation
95 gold deposits is debated. For example, the similar organic gas (e.g., CH_4, C_2H_6)
96 component within fluid inclusions from different mineralization stages (Jin et al.,
97 2016) has been used to suggest there is no genetic relationship between
98 hydrocarbons and gold mineralization, with its spatial association being only
99 coincidental. In contrast, it has been suggested that hydrocarbons can be enriched
100 metals. For example, Au, Zn, and U, with Au reaching ppm levels (Large et al., 2011;
101 Migdisov et al., 2017). The source of Au in Carlin-type gold systems is also debated,
102 with both metal-enriched sedimentary formations (Hofstra and Cline, 2000; Emsbo et
103 al., 2003; Large et al., 2011) and magmatic-hydrothermal activity (Muntean et al.,
104 2011; Large et al., 2016; Zhu et al., 2020) being consider as the progenitor. In both
105 cases Au bearing fluids can interact with liquid oil in the shallow crust (Fetter et al.,
106 2019). Yet, the lack of coeval igneous intrusions near the gold deposits of the
107 Nanpanjiang Basin, as well as elevated $\delta^{34}S$ values of ore-related sulfide minerals (Xie
108 et al., 2018b) are interpreted to indicate basinal derived fluids could have played an
109 important role during mineralization (Gu et al., 2012). The apparent association of
110 gold and organic matter in the Witwatersrand Basin, South Africa (Parnell and

McCready, 2000), the Erickson gold mine, northern British Columbia, Canada (Mastalerz et al., 1995), gold-bearing bitumen in gold deposits at Elliot Lake-Blind River region of Ontario, Canada (Mossman et al., 1993) and Cherry Hill, California (Pearcy and Burruss, 1993) suggest hydrocarbon fluids have entrained gold during migration or entrapped gold from the parent fluid and then promote gold precipitation as a reductant. Additionally, recent experimental data show that oil could either aid gold pre-enrichment or act as the metal carrier before metal precipitation (Zhuang et al., 1998; Migdisov et al., 2017; Crede et al., 2019).

Rhenium and Os are both siderophilic and chalcophilic and commonly are enriched in metal sulfides (e.g., pyrite). The Re-Os radioisotope system has been proven to be a robust tool for determining the timing and duration of sulfide and cogenetic ore mineralization (e.g., Stein et al., 2000; Selby et al., 2009; Hnatyshin et al., 2020). Additionally, Re and Os are also organophilic, and are typically enriched in hydrocarbons (oil, bitumen, pyrobitumen), with the Re-Os isotope systematics recording the timing of liquid oil, pyrobitumen formation, and by inference dry-gas generation (e.g., Selby and Creaser, 2005; Ge et al., 2016; Georgiev et al., 2016; Liu and Selby, 2017; Liu et al., 2018; Georgiev et al., 2019). In order to resolve the spatial relationship between pyrobitumen and Carlin-type gold in the Nanpanjiang Basin, the Laizishan and Banqi paleo-reservoirs and Yata Carlin-type gold deposit were chosen for Re-Os dating of pyrobitumen and gold-bearing pyrite. Integrating our data with previous studies (e.g., petrography, isotope dating, basin modeling, fluid inclusion analysis), the new Re-Os data aid in providing the direct timing of reservoir

evolution, as well as the age of the Carlin-type gold mineralization, and yield insights into the genetic relationship between hydrocarbons and gold mineralization.

2. GEOLOGICAL SETTING

The Nanpanjiang Basin, located at the junction of Guizhou, Yunnan, and Guangxi provinces, occurs within the southwest margin of the South China block (Fig. 1A) (Liu et al., 2016; Yan et al., 2018). The total area of the basin is ~90,000 km^2 and is fault-bounded by the Indochina block, Kangdian area, Jiangnan orogenic belt, and the Qinfang fold belt (Fig. 1A, B) (Liu et al., 2016). The Nanpanjiang Basin records a complex tectonic evolution since the early Paleozoic. Beginning with the formation of the South China block during the Caledonian orogeny (Liu et al., 2001), this region evolved from a rifted basin during the Devonian to a passive continental margin from the early Carboniferous to the early Triassic, the latter controlled by the Hercynian orogeny (Qin et al., 1996; Du et al., 2013; Lai et al., 2014). Associated with the opening of the Ailaoshan Ocean and northward motion of the South China block, northeast-southwest extension resulted in the formation of the Nanpanjiang Basin during the Devonian (Qin et al., 1996; Du et al., 2013). With the closure of the Tethys Ocean and the subduction of Ailaoshan orogenic belt, the Indosinian terrane collided with the South China block during the Middle Triassic (Indosinian orogeny), which led to collision of the Nanpanjiang Basin with the North Vietnam block (Qin et al., 1996; Zaw et al., 2014). Following the Indosinian orogeny, the late Triassic-early Jurassic Yanshanian orogeny resulted in intracontinental deformation of the Nanpanjiang basin (Cai and Zhang, 2009; Zaw et al., 2014).

155 Precambrian to very Early Devonian strata are mostly absent in the Nanpanjiang
156 Basin (Liu et al., 2016). However, the late early Devonian to middle Triassic is well
157 preserved (Du et al., 2013; Liu et al., 2016). Devonian strata mainly consist of
158 sandstone, siltstone, shale, and marlstone with a total thickness of ca. 400 m (Liu et
159 al., 2016). The Carboniferous to Permian is represented by 3000 m of shallow-water
160 platform carbonate in the northwest, and by a deep-water basinal sequence with
161 some shallow water carbonate platforms in the southeast (Fig. 1). The two
162 depositional systems are separated by the Poping thrust fault (F6) (Du et al., 2013).
163 The carbonate platforms mainly consist of bioreef limestone, micrite, and oolitic
164 limestone and breccia, with the basin facies composed of siliceous- and clay-rich
165 units and black mudstone (Liu et al., 2016) (Fig. 2). Some of the Permian strata
166 (Permian Maokou Formation) comprises up to 500 m of pyroclastic rocks related to
167 ~260 Ma Emeishan volcanism (Jin et al., 2016). The Triassic is represented by 6000 m
168 of clastic turbidites that consist of mixed sandstone and mudstone (Liu et al., 2016).
169 Shales and mudstones occur throughout the Devonian to Triassic strata within the
170 Nanpanjiang Basin. Geological survey and geochemical analysis on the potential
171 source rocks found that the Devonian shales of ~2000m thickness, with an organic
172 carbon abundance (TOC) > 1.5 %, are the major hydrocarbon source rock within the
173 basin (Zhao et al., 2006c). Whereas, the Permian to Triassic marlstones and
174 calcareous shale which possess very low TOC (<0.5 %) coupled with a limited
175 distribution have a very poor hydrocarbon generation capacity (Zhao et al., 2006c).
176 The Middle to Late Permian limestone (reef limestone and platform carbonate) are

177 the key paleo-reservoir units, with hydrocarbon shows mainly observed in vugs and
178 on fracture planes (Zhao et al., 2007). In the Laizishan and Banqi domes, solid
179 bitumen is found within vugs and/or along fractures in the Late Permian Wujiaping
180 Formation (Fig. 3). The solid bitumen in the Late Permian Wujiaping Formation is
181 characterized by being insoluble in organic solvents (e.g., carbon disulfide,
182 chloroform), having low H/C ratios (0.17-0.52) and high bitumen reflectance (e.g.,
183 BRo % >2.0 %)(Zhao et al., 2007), indicating the bitumen exhibits a high hydrocarbon
184 maturity and is pyrobitumen (Zhuang et al., 2000; Zhao et al., 2007).

185 Carlin-type gold deposits in the Nanpanjiang Basin are mainly found in the
186 Permian to Triassic carbonate and terrigenous clastic units (Su et al., 2018). The
187 deposits are classified as Stratabound Type, Fault Type, and Compound Type (Gu et
188 al., 2013; Jin et al., 2016). The Stratabound Type gold deposits (Shuiyindong, Nibao,
189 Getang) are distributed within carbonate platform facies and are closely associated
190 with a detachment fault or the regional unconformity between the Permian Maokou
191 and Longtan formations; the Fault Type deposits (Lannigou, Yata, Banqi, Zhesang) are
192 within the basin center and are spatially associated with high-angle thrust faults; the
193 Compound Type deposits (e.g., Bojitian, Zimudang) possess both Fault and
194 Stratabound Type features (Fig. 1). All Carlin-type gold deposits in the Nanpanjiang
195 Basin have similar host rocks (Triassic organic-rich, dark gray to black silty bioclastic
196 limestone and calcareous siltstone), mineral paragenesis (Pre-ore stage: Fe-rich
197 calcite-detrital quartz, Ore stage: vein quartz, pyrite/arsenopyrite, realgar, and vein
198 calcite), and alteration (decarbonatization, silicification, argillization, sulfidation) (Gu

et al., 2013; Su et al., 2018). As noted above, similar to the Carlin-type deposits in Nevada, pyrite is the main host mineral for invisible gold (Su et al., 2018).

Here we focus on the Laizishan and Banqi reservoirs that are spatially associated with the Yata gold deposit (Fig. 3). The pyrobitumen-bearing outcrops are on the southern margin of the Laizishan dome and northern margin of the Banqi dome, ca. 20 km apart. At the Yata deposit, located between the Laizishan and Banqi reservoirs ca. 12 km southwest of the Laizishan dome (Fig. 3), gold-bearing pyrite occurs near the No. 940 mine hole.

3. SAMPLES AND METHODS

Pyrobitumen samples (n = 8) were obtained from outcrops of the Laizishan and Banqi reservoirs for Re-Os analysis (Fig. 3) (see Table 1 for detail). The pyrobitumen was sampled from vugs and fracture surfaces in limestone of the Permian Wujiaping Formation. Pyrobitumen occurrences are typically ~2 to 3 cm wide and ~4 to 6 cm long, dark gray to black, associated with calcite, and have smooth and vitreous surfaces (Fig. 4a, c). Samples LZS-3, LZS-6, and LZS-14 come from two different outcrops in the Laizishan reservoir, ca. 6 km west of Ceheng City. Sample LZS-3 and LZS-6 were collected 3 m apart from a ~8-m-long section. About 2 km to the northeast, sample LZS-14 was collected from an open-pit quarry (Fig. 3). Samples BQ-1, BQ-3, BQ-5, BQ-11, and BQ-12 come from the northern margin of the Banqi paleo-reservoir ~4 km north of Banqi village (Fig. 3). Like the samples from the Laizishan reservoir, all of pyrobitumen from the Banqi reservoir is hosted by the Wujiaping Formation limestone. Samples BQ-1, BQ-3, and BQ-5 were collected from

221 the same outcrop with a sampling interval of about 3 m; samples BQ-11 and BQ-12
222 were taken from an outcrop located ~2 km to the west. All pyrite samples used for
223 Re-Os analysis (*n* = 9) were collected from a ~10-m-long section at 1 m spacings near
224 the No. 940 mine of the Yata gold deposit, ~2 km east of Yata village (Fig. 3) (see
225 Table 2 for details). Similar to other gold deposits in this area (Lannigou and Banqi
226 deposits), all of the pyrite in the Yata gold deposit is hosted in sandstone and
227 siltstone of the Middle Triassic Xinyuan Formation. The pyrite mainly occurs as
228 disseminated small (10-200 μm) euhedral grains (Fig. 4b, d, g), and locally as massive
229 aggregates (Fig. 4e). Microscopically, pyrite and pyrobitumen exhibit a close textural
230 association with pyrite either surrounding or cross cutting the pyrobitumen (Fig. 4b,
231 d, Fig. S5a) (this study; Wu, 2012) and exhibits a narrow (~ 10 - 20 μm) core-rim
232 texture (Fig. 4h, Fig. S5b) (this study; Wu, 2012).

233 For the Re-Os analysis, approximately 0.2 to 1.0 g of pyrobitumen was first
234 separated from each sample. All samples were isolated without metal contact, with
235 the pyrobitumen handpicked under a light microscope. The large pyrobitumen grains
236 were crushed to approximately 1 mm using an agate pestle and mortar. For the pyrite
237 samples, the pyrite-bearing sandstone-siltstone samples were first crushed to 200-
238 300 mesh (40-75 μm). After then, more than 0.5 g of the pure pyrite grains
239 (aggregates) with no host rock were handpicked under the light microscope.

240 The Re and Os isotopic analyses were conducted at the Laboratory for Source
241 Rock and Sulfide Geochemistry and Geochronology, and the Arthur Holmes
242 Laboratory at Durham University following published analytical procedures (Creaser

et al., 1991; Völkening et al., 1991; Shirey and Walker, 1995; Selby et al., 2009). Approximately 150 mg of pyrobitumen and ~400 mg pyrite were dissolved and equilibrated with a known amount of mixed ^{185}Re and ^{190}Os spike solution by inverse aqua regia (3 ml HCl + 6 ml HNO_3) in a Carius tube for 24 hr at 220°C. Osmium was isolated and purified from the acidic digestion medium using solvent ($CHCl_3$) and microdistillation methods. The rhenium was isolated from the Os-extracted solution using a NaOH-acetone solvent extraction and HCl–HNO_3-based anion chromatography. Purified Re and Os were loaded onto Ni and Pt filaments, respectively. The Re was measured using Faraday collectors and Os in peak-hopping mode using a secondary electron multiplier, respectively. Measured Re and Os ratios were corrected for oxide contribution and mass fractionation using $^{185}Re/^{187}Re$ = 0.59738 (Gramlich et al., 1973) and $^{192}Os/^{188}Os$ = 3.08261. All data are blank corrected based on the total procedural blank values of Re (1.6 ± 0.5 pg) and Os (150 ± 30 fg), with an average $^{187}Os/^{188}Os$ ratio of approximately 0.22 ± 0.06 (n = 4). All uncertainties include the propagated uncertainty in the standard, spike calibrations, mass spectrometry measurements, and blanks. The mass spectrometer measurements were monitored by solution reference materials (DROsS and Restd). These solutions yielded values of 0.16083 ± 0.00006 for 50 pg aliquot of DROsS and 0.5990 ± 0.0008 (1SD, n = 5) for a 125 pg aliquot of the Re standard, both of which are in good agreement with those previously reported at Durham University (e.g., Saintilan et al. (2018) and references therein). The Re-Os ages were determined using the $^{187}Re/^{188}Os$ and $^{187}Os/^{188}Os$ ratios together with their total 2σ uncertainty and

associated error correlation, rho, and with the ^{187}Re decay constant of $1.666x10^{-11}a^{-1}$ (Smoliar et al., 1996), via the program Isoplot v. 4.15 (Ludwig, 2008).

In order to determine the gold content of the pyrite samples, eight polished sections were selected for Electron probe microanalysis (EPMA) (Table 3). They were analyzed using a JEOL JXA-8230 electron microprobe at the Laboratory of Microbeam Analysis Technology Limited Company, Wuhan. Prior to analysis, the samples were firstly coated with ca. 20 nm thick conductive carbon film following published analytical procedures (Zhang and Yang, 2016). The abundance of gold (Au), As, Fe, S, Ag, Sb, Zn and Cu in pyrite was determined using an accelerating voltage of 20 kV, analysis diameter of 1 μm and probe current of 20 nA. The peak counting time was 10 s for Cu, S, Fe, Sb, Ag, As, Zn and 120 s for Au. The background counting time was half of the peak counting time. The standards used are Copper (Cu), Pyrite (S, Fe), Antimony (Sb), Silver (Ag), Gold (Au), Gallium Arsenide (As), and Zinc (Zn).

4. RESULTS

4.1 Rhenium–Osmium data for Laizishan and Banqi reservoir pyrobitumen

The Re and Os abundance of the pyrobitumen samples range from 5 to 283 ppb and 209 to 2360 ppt, respectively (Table 1). These values are significantly higher than those of average upper crustal values (Re = 0.2-1 ppb, Os = 31 ppt (Esser and Turekian, 1993; Peucker‐Ehrenbrink and Jahn, 2001)), but similar to previously reported values for pyrobitumen (Ge et al., 2016). The $^{187}Re/^{188}Os$ values of the pyrobitumen range between 67.6 and 683.0 and exhibit a radiogenic $^{187}Os/^{188}Os$ composition of 0.82 to 3.21 (Table 1). The Re-Os isotopic data of the eight

287 pyrobitumen samples yield a Model 3 Re-Os age of 236 ± 36 Ma, with an initial
288 $^{187}Os/^{188}Os$ composition [Os_i] of 0.42 ± 0.28 (Fig. 5). This Model 3 result assumes that
289 the scatter about the best-fit line is a combination of the assigned uncertainties and
290 an unknown, but normally distributed, variation in the $^{187}Os/^{188}Os$ values (Ludwig,
291 2008).

292 **4.2 Rhenium–osmium data for Yata gold deposit pyrite**

293 The Re and Os (^{192}Os) abundances for the pyrite samples are 0.6 to 7.9 ppb and 29
294 to 106 (11–33) ppt, respectively (Table 2). These abundances are similar to pyrite
295 reported in other metal deposits (Lawley et al., 2013; Zimmerman et al., 2014;
296 Hnatyshin et al., 2015; Kelley et al., 2017). The $^{187}Re/^{188}Os$ and $^{187}Os/^{188}Os$ values of
297 the pyrite range from 115.5 to 556.6 and from 1.0 to 2.8, respectively (Table 2). The
298 Re-Os data of the nine samples yield a Model 3 age of 233 ± 42 Ma, with Os_i of 0.59 ±
299 0.26 (Fig. 6).

300 **4.3 Electron probe microanalysis data for Yata gold deposit pyrite**

301 The EPMA data of the pyrite samples which were selected for Re-Os analysis are
302 presented in Table 3. In these samples the abundance of Au, As, Ag, Sb, Zn, and Cu is
303 variable and exhibit the following general trend As > Au > Cu > Zn > Ag > Sb (Table 3).
304 The As and Au abundance ranges from 300 to 58,400 ppm (average = 9400 ppm) and
305 90 to 800 ppm (average = 345 ppm), respectively. For the remaining elements (Ag, Sb,
306 Zn, Cu) the abundances are very low with some analyses below detection limit (Ag up
307 to 300 ppm, average = 130 ppm; Sb = 100 to 200 ppm, average = 118 ppm; Zn = 100
308 to 300 ppm, average = 150 ppm; Cu = 100 to 300 ppm, average = 165 ppm). In

309 agreement to previous studies, the dominant location of the gold is within
310 fine-grained pyrite and narrow pyrite rims (Fig. 4g, h). Although Au could be detected
311 in some pyrite cores, there is a clear decreasing trend of Au abundance from the rim
312 to the core (Fig. 4h).

313 **5. DISCUSSION**

314 **5.1 Timing of dry gas generation in Nanpanjiang Basin**

315 Hydrocarbon generation is a step-by-step process involving the production of liquid
316 oil initially, which with increased temperature thermally cracks to form gas and
317 pyrobitumen (Lewan, 1985). In the Nanpanjiang Basin (i.e., the Banjie, Anran, Balai,
318 Laizishan reservoirs), the solid bitumen exhibits the following characteristics,
319 insoluble in organic solvents (Zhao et al., 2007), low H/C ratio (0.17-0.52) (Zhao et al.,
320 2007), high bitumen reflectance (BRo, %) (2.85-6.25 %) (Zhuang et al., 2000; Zhao et
321 al., 2007), mosaic structure and straight and clear boundary of the bitumen under
322 microscope (Zhao et al., 2007) and organic geochemistry ratios of C_{29}ααα
323 20S/(20S+20R) of 0.62-0.78, C_{29}ββ/(ββ+αα) of 0.31-0.48, and a methylphenanthrene
324 index (MPI-1) of 0.38-1.00 (equal to a Ro of 1.7-2.1%) (Table S5)(Wu, 2012). These
325 features indicate that the solid bitumen is high hydrocarbon maturity pyrobitumen
326 that formed from the cracking of liquid oil (Seifert and Moldowan, 1986; Chen and
327 Jin, 1995; Peters et al., 2005; Zhao et al., 2007; Wu, 2012). Any gas reservoirs formed
328 as a result of the thermal cracking of oil in the Nanpanjiang Basin are considered to
329 have been lost through uplift and erosion. However, methane is present and
330 comprises more than 80 % of the gas phase in gas-bearing fluid inclusions in existing

reservoirs (Gu et al., 2012), and occur with coeval aqueous fluid inclusions that yield an average homogenization temperature (T_h) > 150°C (Zhao et al., 2006a; Gu et al., 2012).

All of the pyrobitumen Re-Os data from the Laizishan and Banqi reservoirs collectively yield a Re-Os age of 236 ± 36 Ma (*n* = 8, initial $^{187}Os/^{188}Os$ ratio [Os_i] = 0.42 ± 0.28, Mean Squared Weighted Deviates [MSWD] = 871) (Fig. 5). The large age uncertainty and MSWD value suggest that the sample set does not fully meet the criteria for developing a robust isochron, which requires that (1) all samples formed contemporaneously, (2) all samples possess the same Os_i value, and (3) the isotope systematics have not been disturbed (Cohen et al., 1999; Kendall et al., 2009). Calculated Os_i values using the Re-Os age of 236 Ma show that samples LZS-3, BQ-5, and LZS-6 have less-radiogenic values (0.17, 0.32, and 0.36, respectively), compared to the remaining samples that possess more similar and radiogenic Os_i values (0.49-0.56; avg Os_i = 0.52 ± 0.03), with the exception of BQ-11 (0.43; including BQ-11 avg Os_i = 0.50 ± 0.05) (Table.1). As such, the scatter about the best-fit line of the Re-Os data is a function of the data set having variable Os_i values (e.g., samples LZS-3, BQ-5, LZS-6). Although hard to confirm, the relatively long intervals of both initial oil generation from the source rock and the later pyrobitumen and gas generation during oil cracking, could result in the samples not being formed contemporaneously, and as a result could cause variations in Os_i, as well as the large age uncertainty and MSWD values (Lillis and Selby, 2013; Ge et al., 2016). The Re-Os data for samples BQ-1, 3, 11, 12, and LZS-14 yield a Re-Os age of 228 ± 16 Ma (*n* = 5, Os_i = 0.56 ± 0.13,

MSWD = 47) (Fig. 5). Although an isochron age determined from two samples is not a robust reflection of the true geologic age (Ludwig, 2008), the Re-Os data for samples BQ-5 and LZS-6 yield a Re-Os age of 229.7 ± 4.0 Ma (Os_i = 0.39 ± 0.03) (Fig. 5), which is similar to that determined for samples BQ-1, BQ-3, BQ-11, BQ-12, and LZS-14.

Basin modelling of strata in the Yang 1 well, ~15 km southeast of our study area (Fig. 1), suggests that the Devonian source rocks entered the oil window (~2 km depth, Ro: 0.6-1.0 %) during the Late Carboniferous, with peak oil generation occurring in the Permian (Zhao et al., 2006b). However, rapid subsidence driven by the Indochina-South China collision from the Late Permian to Early Triassic resulted in the Permian limestone being buried to >5 km (Zhao et al., 2006b; Zaw et al., 2014) (Fig. 7). Burial modelling and hydrocarbon maturation analysis of the Devonian shale in the Nanpanjiang Basin indicate that the shale began to generate dry gas during the Middle Triassic (Zhou, 1999). According to the temperature gradient in South China (Hu et al., 2000), temperatures of the Late Permian reservoir could have reached more than 200°C, which is consistent with the homogenization temperatures (> 150 °C) for aqueous fluid inclusions coeval with methane-dominated fluid inclusions (Zhao et al., 2006a; Gu et al., 2012). Such temperatures would have resulted in the thermal cracking of any liquid oil. In summary, basin modelling indicates that oil generation and accumulation happened before the Middle Triassic, with thermal cracking of the reservoir oil occurring following rapid subsidence of the Nanpanjiang Basin after the mid-Triassic (Zhao et al., 2006b).

374 Studies have found that the Re-Os systematics of highly mature hydrocarbons in
375 the Bighorn Basin, USA (Lillis and Selby, 2013), and bitumen in the North Hebei
376 depression, China (Li et al., 2017), may exhibit disturbance. Moreover, Re-Os dating
377 of pyrobitumen that formed contemporaneously with methane in the
378 Majiang-Wanshan reservoir, Xuefeng uplift, the Micang Shan reservoir, northern
379 Sichuan Basin as well as the Ziyang-Weiyuan-Anyue gas field, central Sichuan Basin
380 in the South China block, show that the pyrobitumen Re-Os age coincides with the
381 timing of gas generation (Ge et al., 2016; Ge et al., 2018; Shi et al., 2020). The Re-Os
382 age of 228 ± 16 Ma determined here for pyrobitumen from the Laizishan and Banqi
383 reservoirs is younger than that inferred for liquid oil generation (Zhao et al., 2006b),
384 but is within uncertainty and in agreement with the estimated timing of the thermal
385 cracking of liquid oil, thus further suggesting that pyrobitumen Re-Os ages yield the
386 timing of gas, not oil, generation.

387 **5.2 Timing of gold mineralization in the Nanpanjiang Basin**

388 Establishing the mineralogical residence of the gold and its distribution within
389 Carlin-type deposits has been an on-going challenge since the discovery of the
390 deposit type in the 1960s (Zhang, 1997; Bidari and Aghazadeh, 2018; Cline, 2018).
391 Gold could be contained within chalcopyrite and sphalerite (Wells and Mullens,
392 1973), cinnabar, illite and quartz (Bakken et al., 1989; Cline et al., 2005) in this
393 deposit type. However, because of both scarcity and low gold contents of these
394 minerals, they are not considered to be the major gold host. It is now generally
395 accepted that invisible gold in Carlin-type deposits is encapsulated in sulfides and

clays (Hausen, 2000) and that pyrite is the most common gold-bearing sulfide (Au abundance could exceed 1000 ppm) (Cline et al., 2005; Cline, 2018; Su et al., 2018; Xie et al., 2018a). Although the majority of gold in Carlin-type systems in both Nevada and the Nanpanjiang Basin is ionically bound in the pyrite lattice either as micrometer-scale (<10 μm) grains or within rims of otherwise gold-poor pyrite (Fig. 4g, h) (Su et al., 2012; Cline, 2018), in the Nanpanjiang Basin gold-bearing pyrite is texturally and chemically distinct from that of gold-bearing pyrite in Nevada. For example, ore pyrite in Carlin-type systems of Nevada occurs as rims or interstitial grains and can be readily observed under the microscope. In contrast, in the Nanpanjiang Basin, auriferous pyrite rims are indistinguishable microscopically from the pyrite core because of similar color, relief, and reflectivity. Yet, textural characteristics are however better distinguished by BSE imagery (Fig. 4h), EPMA, and laser ablation-ICP-MS analyses (Xie et al., 2018a). In addition to gold, the rim of pyrite in the Carlin-type systems of Nevada are enriched in As, Hg, Tl, Cu, and Sb, relative to the core (Xie et al., 2018a). Although all of these elements are detected in ore pyrite of the Nanpanjiang Basin, the concentrations are much lower (Table 3) (Xie et al., 2018a). In summary, the morphology and chemical differences of gold-bearing pyrite from Carlin-type deposits in Nevada and those in the Nanpanjiang Basin suggest that the two systems formed from fluids having different characteristics (Xie et al., 2018a). In the Nanpanjiang Basin, subtle variations both in morphology and geochemistry features in the pyrite core and rim indicate they were formed during one continuously evolving hydrothermal event (Xie et al., 2018a) and thus dating the

418 gold-bearing pyrite could help constrain the timing related to this hydrothermal
419 event and the formation of the gold deposits.

420 All of the Re-Os data for the pyrite from the Yata gold deposit yield an age of 233 ±
421 42 Ma (n = 9, Os_i = 0.59 ± 0.26, MSWD = 59) (Fig. 6). Importantly, the large age
422 uncertainty and MSWD value are controlled by two samples (YT-42 and YT-46) that
423 deviate from the best-fit line (Fig. 6). The calculated Os_i using the Re-Os age of 233
424 Ma yields values of 0.35 and 0.81 for samples YT-46 and YT-42, respectively (Table 2).
425 The Re-Os data for the remaining seven samples produces a more precise Re-Os age
426 of 218 ± 25 Ma (n = 7, Os_i = 0.67 ± 0.16) and lower MSWD (8.1) (Fig. 6). However, the
427 Os_i values calculated at 218 Ma for samples YT-46 (0.42) and YT-42 (0.93) are still
428 significantly different (Table 2). The later maybe explained by impurities in mineral
429 separates, open-system behavior of the Re-Os isotopic system (Nakai et al., 1993),
430 mixing of different generations of sulfide and / or prolonged mineralization
431 (Hnatyshin et al., 2015; Hnatyshin et al., 2020). Given that the sampled pyrite grains,
432 for example YT43 and YT42, are mixture of core and rim pyrite (micro-meter scale
433 that are impossible to separate (Fig. 4h)) that formed as a result of a continuously
434 evolving hydrothermal event (Xie et al., 2018a), a prolonged mineralization duration
435 and / or mixing of different generations of pyrite, may cause the differences
436 observed in the Os_i compositions of pyrite from the Yata deposit, which ultimately
437 results in the large age uncertainty.

438 The pyrite samples from the Yata deposit were collected from siltstone of the
439 Xinyuan Formation of the Middle Triassic Anisian stage. Although the pyrite Re-Os

age of 218 ± 25 Ma has a relatively large uncertainty, the nominal Re-Os age is in good agreement with (1) a Rb-Sr age of 212.8 ± 4.6 Ma determined on hydrothermal, gold-bearing, fine-grained (3-5 µm) illite from the Yata deposit (Table S1, Fig. S1a) (Jin, 2017); (2) an *in situ* SIMS U-Pb age of 213.6 ± 5.4 Ma for hydrothermal rutile from the Zhesang gold deposit, ~100 km south of Yata (Fig. 1) (Pi et al., 2017); and (3) Re-Os arsenopyrite ages of 204 ± 19 Ma, 206 ± 22 Ma and 235 ± 33 Ma for the Lannigou, Jinya, and Shuiyindong deposits in the Nanpanjiang Basin (Chen et al., 2015). Collectively, the Re-Os, Rb-Sr, and U-Pb Late Triassic ages may indicate the beginning of Carlin-type gold mineralization in the Nanpanjiang Basin. Whereas older isotope ages, for example Rb-Sr ages (235 ± 9.3 Ma)on coarse-grained (5-10 µm) illite for the Yata deposit (Table S1, Fig. S1b) (Jin, 2017), Rb-Sr ages on fluid inclusions in the Jinya deposit (276 ± 28 Ma; Wang, 1992) and the Lannigou deposit (259 ± 27 Ma; Hu et al., 1995), which are in some cases older than the host sedimentary strata (Middle Triassic), do not record the time of mineralization. Younger ages (<200 Ma), for example an Ar-Ar sericite age for the Lannigou deposit (194.6 ± 2 Ma; Chen et al., 2009), Rb-Sr age for realgar-bearing quartz from the Yata deposit (148.5 ± 4.1 Ma)(Table.S2, Fig. S2) (Jin, 2017), and Sm-Nd ages on calcite and fluorite from the Shuiyindong, Nibao, and Shitouzhai deposits (122-180 Ma) (Table S3, S4; Fig. S3, S4)(Su et al., 2009; Gu et al., 2012; Jin, 2017), likely record hydrothermal activity that post-dates the main episode of gold mineralization or its termination (Fig. 8) (Su et al., 2009; Gu et al., 2012; Jin, 2017). The latter interpretation is further supported by petrography, EPMA, and XRD analysis that show that the hydrothermal sericite in the

462 Yata deposit is bereft of gold and post-dates gold deposition (Chen et al., 2009). As
463 such, the Early Jurassic (ca. 195 Ma) Ar-Ar sericite age for the Lannigou deposit could
464 represent the waning stages of hydrothermal activity of the Carlin-type gold systems
465 in the region.

466 **5.3 Relationship between hydrocarbons and gold mineralization**

467 It is well documented that metals are associated with crude oil and solid bitumen
468 in many sedimentary basins (Kesler et al., 1994; Wilson and Zentilli, 2006; Emsbo and
469 Koenig, 2007; Gu et al., 2010). The oil and bitumen in the MVT Pb-Zn deposits are
470 considered to be the source for the reduced sulfur required to precipitate the sulfide
471 ores through either direct release of organically bound sulfur in Cincinnati arch, USA
472 (Kesler et al., 1994) or thermochemical reduction of sulfate from basinal fluids or
473 evaporates in Pine Point, Canada (Powell and Macqueen, 1984). Paragenetic and
474 geochemical analysis of the manto-type copper deposits, central Chile suggest
475 pyrobitumen may act as a reductant for the mineralizing fluids (Wilson and Zentilli,
476 2006). The Laser ablation ICP-MS analyses on the bitumen in the EI Rodeo deposit,
477 USA, which showed that bitumen could contain up to 100 ppm Au, were used to
478 suggest Au and associated metals could be remobilized and transported as
479 organo-metallic compounds during oil generation and migration (Emsbo and Koenig,
480 2007). In addition, more recent empirical evidence suggests that petroleum may
481 have acted as an important fluid during ore formation (Migdisov et al., 2017) and this
482 has been an overlooked frontier in ore genesis research (Williams-Jones et al., 2009).
483 In a water-oil-rock system, gold has been experimentally shown to predominantly

484 enter the oil phase (Zhuang et al., 1998). Furthermore, recent experiments show
485 metal (Zn, Au, U) abundance in crude oils increases from 100 to 200 - 250°C, peaking
486 at ca. 200 - 250 °C (50 ppb for Au), and then begins to decrease at > 250°C - 300 °C
487 (Migdisov et al., 2017). Although largely qualitative, this result provides insight into
488 the behavior of metals in liquid hydrocarbons and indicates that liquid hydrocarbons
489 have the potential to mobilize and concentrate metals. Specifically the experimental
490 conditions show that as a liquid oil begins to convert to pyrobitumen and natural gas
491 at elevated temperatures (> 160 °C) (Williams-Jones et al., 2009; Zhu et al., 2013),
492 the decrease in metal abundance in the hydrocarbon (Migdisov et al., 2017)
493 coincides with the conditions of thermal cracking of oil. In summary, the experiment
494 indicates that metals (Zn, Au, U) can be enriched in liquid oil, but these metals will be
495 released to the fluid phase during the thermal cracking of oil (Zhuang et al., 1998;
496 Emsbo and Koenig, 2007; Migdisov et al., 2017; Crede et al., 2019).

497 Homogenization temperatures (T_h) of fluid inclusions in diagenetic calcite from the
498 Permian hydrocarbon reservoirs in the Nanpanjiang Basin range from ~70°C to 220°C
499 (Zhao et al., 2006a; Gu et al., 2012). Specifically, early stage aqueous fluids inclusions
500 that are coeval with the oil-bearing fluid inclusions are characterized by low T_h
501 (73-87°C, mean 80°C). In contrast, late stage aqueous fluid inclusions that are coeval
502 with the methane-dominated inclusions possess high T_h (110-180°C, mean > 150°C),
503 and reflect the thermal cracking of liquid oil (Gu et al., 2012) (Fig. 9).

504 Fluid inclusion analysis from different mineralization stages of the Carlin-type gold
505 deposits in the Nanpanjiang Basin show a decreasing trend in T_h data from ca. 230°C

506 during the gold-bearing pyrite stage to ca. 150°C during the post-gold, vein
507 realgar-calcite stage (Hu et al., 2002; Gu et al., 2012; Su et al., 2018). The
508 temperatures of thermal cracking of oil and main gold mineralization that occurred in
509 the Nanpanjiang Basin could be a continuous process with oil cracking being
510 post-dated by pyrite formation during the increase in temperature. In addition,
511 similar mass chromatogram characteristics of sterane and terpane (for example
512 GAM/H_{30} ratio (0.14 vs 0.14), H_{32} S/(R+S) ratio (0.51 vs 0.52) and similar V shape
513 distribution of C_{27}, C_{28}, C_{29} steranes with C_{29} sterane exhibiting the highest
514 abundance) for pyrobitumen either from the paleo-reservoirs or gold deposits from
515 Nanpanjiang Basin indicate they are from same source (Table S5) (Wu, 2012). Both
516 pyrobitumen and pyrite occur in the pore spaces of the limestone in the Laizishan
517 reservoir (Fig. 4b, d) with pyrite observed to cross cut pyrobitumen in the
518 Shuiyindong gold deposits, Nanpanjiang Basin (Fig, S5a) (Wu, 2012). All the above
519 features indicate that pyrobitumen formation by thermal cracking as well as gold
520 mineralization is broadly coeval, including the possibility that the pyrobitumen
521 formed slightly earlier than the gold-bearing pyrite. Our Re-Os dating supports this
522 temporal relationship between pyrobitumen formation (228 ± 16 Ma) and gold
523 mineralization (218 ± 25 Ma), in which the pyrobitumen is nominally older, but with
524 both events occurring during peak burial temperatures (>200°C) within strata of the
525 Nanpanjiang Basin. The proposed origin of the gold involving the thermal cracking of
526 liquid oil is potentially also supported by the similar Os_i values of the pyrobitumen
527 (0.58-0.72) and pyrite (0.59-0.76). In our model, during burial of the Permian

528 reservoir to more than 5 km (>150 °C condition) the oil thermally cracked, with the
529 spatially associated fluids incorporating not only the gold, but also the osmium
530 isotope composition from the thermally cracked oil.

531 Given that gold in Carlin-type gold deposits worldwide mainly resides in pyrite
532 (Cline, 2018; Muntean, 2018a; Su et al., 2018), the mechanism that leads to
533 precipitation of the gold-bearing pyrite is important to consider. Petrographic and
534 geochemical evidence from the northern Carlin trend indicate sulfidation between
535 Fe-dolomite and Au and H_2S rich ore fluid was the most important mechanism of
536 gold deposition in Carlin-type deposits (Emsbo et al., 2003). As mentioned above, the
537 major host rock at the Lannigou and Yata gold deposits is Fe-rich calcareous and
538 dolomitic siltstone. Scanning electron microscopy-energy dispersive spectroscopy
539 (SEM-EDS) of samples from the Lannigou deposit indicate that iron concentrations in
540 the Fe dolomite range between 11 and 17 wt % (Xie et al., 2018a), which via leaching
541 by hydrothermal fluids could have provided sufficient iron for pyrite formation.
542 Lithogeochemical studies of the Shuiyindong gold deposits suggests that the gold
543 and associated trace elements were also transported in H_2S-rich fluids (Su et al., 2009;
544 Su et al., 2018). Together with the observed replacement of ferroan calcite and
545 dolomite in the host rocks by arsenian pyrite and illite, gold-bearing ore pyrite is also
546 attributed to have formed from a H_2S-rich ore fluid via sulfidation of local Fe-bearing
547 minerals in the Nanpanjiang Basin (Su et al., 2018).

548 Although a magmatic source of sulfur for the gold deposits is considered (Xie et al.,
549 2018b), the lack of coeval intrusions and only being distal to the gold deposits may

indicate the possibility of a sedimentary derived sulfur component In the Nanpanjiang Basin (Hu et al., 2002). As to the formation of the H_2S, the broad range of S isotope values in the Carlin type gold deposits lead to proposal of several mechanisms, such as the dissolution of diagenetic pyrite, desulfidation of pyrite to pyrrhotite, thermochemical sulfate reduction and the destruction of organosulfur compounds (Emsbo et al., 2003; Cline et al., 2005; Large et al., 2011). The $\delta^{34}S$ values of ore pyrite from gold deposits in our study area are also variable (Su et al., 2018). Previous studies show ore pyrite $\delta^{34}S$ values of 7.3 - 12.6‰, -2.3 - 8.0‰, and ca. 9.0‰ in the Laizishan, Yata and Banqi gold deposits, respectively (Zhang, 1997; Su et al., 2018). Although some sulfur isotope data overlap with the range of magmatic sulfur (-2.5 - 5.1‰) (Seal, 2006), the overall variability of the sulfur isotope values suggests that H_2S in the ore fluids was probably derived from sedimentary rocks. Therefore, the thermochemical sulfate reduction (TSR), with the reaction between organic matter (oil and gas) and sulfate at elevated temperatures (>140^{o} C) with the formation of carbonate (CO_3^{2-}), carbon dioxide (CO_2) and H_2S, could be a significant process (Machel, 2001; Cai et al., 2004; Hao et al., 2015). Because the bond energy of ^{32}S-O is lower than that of ^{34}S-O, more $^{32}SO_4^{2-}$ relative to $^{34}SO_4^{2-}$ will take part in the TSR process, leading to the sulfide having a relatively lighter sulfur isotope composition compared with coeval sulfate (Zhu et al., 2005). Previous work has found that the sulfur isotope difference between sulfide and sulfate ($\Delta^{34}S$) decreases from ~20 to 10 ‰ as temperature increases from 100 ^{o}C to >200 ^{o}C (Machel et al., 1995). Sulfur isotope data for the ore-stage pyrite ($\delta^{34}S$ ~20 ‰) in the Post/Betze

572 gold deposit and Paleozoic seawater sulfates represented by stratiform barite
573 (20-35‰) in Nevada, indicate that TSR may be an important mechanism for the
574 source of sulfur (Arehart et al., 1993; Emsbo and Hofstra, 2003). Similar to the
575 Carlin-type gold deposits in Nevada, a stratiform barite deposit (e.g., Zhenning
576 deposit, ~100 km north of Yata gold deposit) is present in Devonian strata within the
577 Nanpanjiang Basin, which exhibits a mean $\delta^{34}S$ value of ca. 37‰ (Hu et al., 2002; Gao
578 et al., 2017). The sulfur isotope values of the hydrothermal pyrite in the Lannigou
579 and Yata gold deposits (4.7 to 12.0 ‰, (Zhang et al., 2003; Su et al., 2018)) are lighter
580 than those of seawater sulfate in the Triassic (ca. 10-15‰) (Claypool et al., 1980) and
581 that of barite from the Zhenning deposit. In addition to Carlin-type gold deposits, the
582 pyrite sulfur isotope values for other sediment-hosted gold deposits worldwide show
583 a similar pattern with the contemporaneous seawater sulfate curve, in which $\delta^{34}S$
584 values are ca. 15 to 20 ‰ lower than that of coeval seawater sulfate, considered by
585 most workers to reflect the reduction of seawater sulfate (Chang et al., 2008). In
586 summary, the lighter $\delta^{34}S$ value of the pyrite in the gold deposits, compared with
587 that of coeval seawater sulfate or the barite, may record TSR processes during the
588 gold-bearing pyrite formation in the Nanpanjiang Basin. Sulfur and carbon isotope
589 analysis of the hydrogen sulfide, carbonate, and calcite in the H_2S-rich natural gas
590 field in the South China block indicate that the H_2S could be derived via TSR between
591 the thermally cracked gas and sulfate (Cai et al., 2004; Zhu et al., 2005; Hao et al.,
592 2015). Moreover, a positive shift in the $\delta^{13}C$ value of methane, which is isotopically
593 heavier than the CO_2, suggests that the methane is the major reactant for the TSR

process in a high C_1/C_{1-6} ratio (>0.95) environment (Worden and Smalley, 1996; Pan et al., 2006; Cai et al., 2013). In the Nanpanjiang Basin, the much higher basin burial temperature (>200^{o} C) led to the thermal cracking of liquid oil into pyrobitumen and methane. Laser Raman spectroscopic analyses of fluid inclusions from calcite in strata of the Laizishan reservoir find CH_4 to be the predominant gas (Gu et al., 2007b). The negative relationship between CO_2 and CH_4 volume in fluid inclusions of the Laizishan reservoir (Gu et al., 2007a) also supports the premise that CH_4 could be involved in the TSR process (Fig. 9). Collectively, the above data support CH_4-dominated TSR in the Nanpanjiang Basin, as also inferred for the Carlin-type gold deposits in the study area.

Integrating all the above data, the relationship between the different types of hydrocarbons (oil and gas) and the formation of the Carlin type gold deposits in the Nanpanjiang Basin is summarized below (Fig. 9). From the Late Carboniferous to Early Triassic, the Devonian source rocks underwent burial and entered the oil window (~120 ^{o}C). During the hydrocarbon (oil) expulsion and migration process from the source to the reservoir, the liquid oil absorbed metals (including Au) sourced from either sedimentary rocks (Hofstra and Cline, 2000) or igneous activity (Zhu et al., 2020)(Fig. 9a). Rapid subsidence driven by the Indochina-South China collision from the Late Permian to Early Triassic resulted in burial of the Permian reservoir to >5 km with temperatures reaching more than 200°C, which led to the thermally cracking of liquid oil and the generation of the pyrobitumen and gas (methane dominated) during the Late Triassic (Fig. 9b). Then, a methane dominated TSR process began and

616 resulted in an increase of reduced sulfur (H_2S) in the fluid. At the same time, the gold
617 released during the cracking of the oil formed a bisulfide complex ($Au(HS)^0$/$Au(HS)_2^-$)
618 with the sulfur in the fluid (Fig. 9b). Finally, when the Au and H_2S rich ore fluid
619 reached the Triassic Fe-rich calcareous and dolomitic siltstone in the Nanpanjiang
620 Basin, sulfidation between bisulfide and iron finally caused the formation of the
621 disseminated gold-bearing pyrite (gold deposit) (Fig. 9c).
622
623 **6. CONCLUSIONS**
624 Integrating Re-Os isotope pyrobitumen and gold-bearing pyrite data, this study
625 quantitatively constrains the evolution of hydrocarbon (oil and gas) and gold
626 mineralization in the Nanpanjiang Basin. The Re-Os age for the highly mature
627 pyrobitumen from the Laizishan and Banqi reservoirs (228 ± 16 Ma) coincides with
628 results of basin modelling for the Nanpanjiang Basin, suggesting that the
629 pyrobitumen and dry gas formed during the early Late Triassic through the thermal
630 cracking of liquid oil. The broadly identical Re-Os age for gold-bearing pyrite from the
631 Yata deposit (218 ± 25 Ma), which is in agreement with *in situ* SIMS U-Pb rutile (213.6
632 ± 5.4 Ma), Re-Os arsenopyrite (204 ± 19 Ma - 235 ± 33 Ma), and Rb-Sr illite (212.8 ±
633 4.6 Ma) ages for other Carlin-type gold deposits in the Nanpanjiang Basin, further
634 supports a model for gold mineralization during the Late Triassic.
635 The contemporaneity of the Re-Os pyrobitumen and gold-bearing pyrite ages (228
636 ± 16 and 218 ± 25 Ma) obtained in this study, coupled with recent experimental data
637 highlighting the uptake and release of metals from hydrocarbons and fluid inclusion

638 data for both hydrocarbon reservoir and gold deposits in the Nanpanjiang Basin,
639 suggest that methane-dominated TSR may be one key formational mechanism for
640 the Carlin-type gold deposits in this basin (Fig. 9). In our model, the produced
641 methane from the thermal cracking of oil reacted with sulfate, resulting in an
642 increase in reduced sulfur (H_2S) in the fluid. At the same time, the gold released from
643 the oil complexed with the sulfur ($Au(HS)^0$/ $Au(HS)_2^-$) in ore bearing fluid. Finally,
644 when the Au and H_2S rich ore fluid reached the Triassic Fe-rich strata in the
645 Nanpanjiang Basin, sulfidation between bisulfide and iron caused the formation of
646 the gold-bearing pyrite mineralization.
647
648 **ACKNOWLEDGMENTS**
649 This work was supported by the National Natural Science Foundation of China
650 (No.41802168, 41672140, 41372140), the PetroChina Innovation Foundation
651 (No.2016D-5007-0103), the Program of Introducing Talents of Discipline to
652 Universities (No.B14031), the Outstanding Youth Funding of Natural Science
653 Foundation of Hubei Province (No. 2016CFA055), and the Fundamental Research
654 Fund for the Central Universities, China University of Geosciences (Wuhan, No.
655 CUG180617, CUGCJ1820, CUGCJ1712), and Open Topic Fund from Key Laboratory of
656 Tectonics and Petroleum Resources of Ministry of Education (TPR-2018-11). Science
657 and technology project of Guizhou province (No. [2018]1065). DS acknowledges the
658 Total Endowment Fund and the Dida Scholarship from CUG Wuhan. We also thank

John Slack, Balz Kamber, David van Acken and one anonymous reviewer for providing insightful comments and suggestions that improved this manuscript.

REFERENCES

Anderson, G.M., 1975. Precipitation of Mississippi Valley-type ores. Economic Geology, 70: 937-942.

Arehart, G.B., Eldridge, C.S., Chryssoulis, S.L., Kesler, S.E., 1993. Ion microprobe determination of sulfur isotope variations in iron sulfides from the Post/Betze sediment-hosted disseminated gold deposit, Nevada, USA. Geochimica et Cosmochimica Acta, 57(7): 1505-1519.

Bakken, B.M., Hochella, M.F., Marshall, A., Turner, A., 1989. High-resolution microscopy of gold in unoxidized ore from the Carlin mine, Nevada. Economic Geology, 84(1): 171-179.

Bidari, E., Aghazadeh, V., 2018. Pyrite from Zarshuran Carlin-type gold deposit: Characterization, alkaline oxidation pretreatment, and cyanidation. Hydrometallurgy, 179: 222-231.

Cai, C. et al., 2004. Methane-dominated thermochemical sulphate reduction in the Triassic Feixianguan Formation East Sichuan Basin, China: Towards prediction of fatal H_2S concentrations. Marine and Petroleum Geology, 21(10): 1265-1279.

Cai, C., Zhang, C., He, H., Tang, Y., 2013. Carbon isotope fractionation during methane-dominated TSR in East Sichuan Basin gasfields, China: A review. Marine and Petroleum Geology, 48: 100-110.

Cai, J.-X., Zhang, K.-J., 2009. A new model for the Indochina and South China collision during the Late Permian to the Middle Triassic. Tectonophysics, 467(1): 35-43.

Chang, Z., Large, R.R., Maslennikov, V., 2008. Sulfur isotopes in sediment-hosted orogenic gold deposits: Evidence for an early timing and a seawater sulfur source. Geology, 36(12): 971-974.

Chen, M., Huang, Q., Hu, Y., Chen, Z., Zhang, W., 2009. Genetic types of phyllosilicate (micas) and its ^{39}Ar-^{40}Ar dating in Lannigou gold deposit, Guizhou Province, China. Acta Mineralogica Sinica, 29(3): 353-362.

Chen, M., Mao, J., Li, C., Zhang, Z., Dang, Y., 2015. Re–Os isochron ages for arsenopyrite from Carlin-like gold deposits in the Yunnan–Guizhou–Guangxi “golden triangle”, southwestern China. Ore Geology Reviews, 64(1): 316-327.

Chen, Z., Jin, K., 1995. Organic petrology characteristics of nature sollid bitumens. Coal Geology & exploration, 23(4): 18-22.

Claypool, G.E., Holser, W.T., Kaplan, I.R., Sakai, H., Zak, I., 1980. The age curves of sulfur and oxygen isotopes in marine sulfate and their mutual interpretation. Chemical Geology, 28: 199-260.

Cline, J.S., 2018. Nevada’s Carlin-type gold deposits: What we’ve learned during the past 10 to 15 years. In: Muntean, J.L. (Ed.), Diversity in Carlin-style gold deposits. Society of Economic Geologists Special Publications, v.20, pp. 7-37.

Cline, J.S., Hofstra, A.H., Muntean, J.L., Tosdal, R.M., Hickey, K.A., 2005. Carlin-type gold deposits in Nevada: Critical geologic characteristics and viable models. Economic Geology, 100th anniversary volume: 451-484.

Cohen, A.S., Coe, A.L., Bartlett, J.M., Hawkesworth, C.J., 1999. Precise Re–Os ages of organic-rich mudrocks and the Os isotope composition of Jurassic seawater. Earth and Planetary Science Letters, 167(3): 159-173.

699 Creaser, R., Papanastassiou, D., Wasserburg, G., 1991. Negative thermal ion mass spectrometry of
700 osmium, rhenium and iridium. Geochimica et Cosmochimica Acta, 55(1): 397-401.
701 Crede, L.-S. et al., 2019. Crude oils as ore fluids: An experimental in-situ XAS study of gold partitioning
702 between brine and organic fluid from 25 to 250°C. Geochimica et Cosmochimica Acta, 244:
703 352-365.
704 Du, Y. et al., 2013. The basin translation from Late Paleozoic to Triassic of the Youjiang Basin and its
705 tectonic signification. Geological Review, 59(1): 1-11.
706 Emsbo, P., Hofstra, A.H., 2003. Origin and significance of postore dissolution collapse breccias
707 cemented with calcite and barite at the Meikle gold deposit, northern Carlin trend, Nevada.
708 Economic Geology, 98(6): 1243-1252.
709 Emsbo, P., Hofstra, A.H., Lauha, E.A., Griffin, G.L., Hutchinson, R.W., 2003. Origin of high-grade gold ore,
710 source of ore fluid components, and genesis of the Meikle and neighboring Carlin-type
711 deposits, northern Carlin trend, Nevada. Economic Geology, 98(6): 1069-1105.
712 Emsbo, P., Koenig, A.E., 2007. Transport of Au in petroleum: Evidence from the northern Carlin trend,
713 Nevada, Dublin. Millpres, Proceedings of the 9th Biennial SGA Meeting, Dublin, pp. 695.
714 Esser, B.K., Turekian, K.K., 1993. The osmium isotopic composition of the continental crust.
715 Geochimica et Cosmochimica Acta, 57(13): 3093-3104.
716 Fetter, N. et al., 2019. Lead isotopes as tracers of crude oil migration within deep crustal fluid systems.
717 Earth and Planetary Science Letters, 525: 115747.
718 Fuchs, S., Williams-Jones, A.E., Jackson, S.E., Przybylowicz, W.J., 2016. Metal distribution in
719 pyrobitumen of the Carbon Leader Reef, Witwatersrand Supergroup, South Africa: Evidence
720 for liquid hydrocarbon ore fluids. Chemical Geology, 426: 45-59.
721 Gao, J. et al., 2017. Forming mechanism analysis of the abnormally high $\delta^{34}S$ baryte deposits: A case
722 study from the Zhenning–Ziyun large Devonian baryte deposits, Guizhou Province, China.
723 Geomicrobiology Journal, 34(6): 481-488.
724 Ge, X., Shen, C., Selby, D., Deng, D., Mei, L., 2016. Apatite fission-track and Re-Os geochronology of the
725 Xuefeng uplift, China: Temporal implications for dry gas associated hydrocarbon systems.
726 Geology, 44(6): 491-494.
727 Ge, X. et al., 2018. Neoproterozoic-Cambrian petroleum system evolution of the Micang Shan uplift,
728 northern Sichuan Basin, China : Insights from pyrobitumen Re-Os geochronology and apatite
729 fission track analysis. AAPG Bulletin, 102(8): 1429-1453.
730 Georgiev, S.V. et al., 2016. Re–Os dating of maltenes and asphaltenes within single samples of crude
731 oil. Geochimica et Cosmochimica Acta, 179: 53-75.
732 Georgiev, S.V. et al., 2019. Comprehensive evolution of a petroleum system in absolute time: The
733 example of Brynhild, Norwegian North Sea. Chemical Geology, 522: 260-282.
734 Gramlich, J.W., Murphy, T.J., Garner, E.L., Shields, W.R., 1973. Absolute isotopic abundance ratio and
735 atomic weight of a reference sample of rhenium. Journal of Research of the National Bureau
736 of Standards - A. Physics and Chemistry, 77A(6): 691-698.
737 Gu, X., Li, B., Fu, S., Xu, S., Dong, S., 2007a. Physicochemical properities of hydrocarbon-bearing fluids
738 in the Youjiang Basin, South China. Bulletin of Mineralogy Petrology and Geochemistry, 26(3):
739 214-217.
740 Gu, X., Li, B., Xu, S., Fu, S., Dong, S., 2007b. Characteristics of hydrocarbons bearing ore forming fluids
741 in the Youjiang Basin, South China: Implications for hydrocarbon accumulation and ore
742 mineralization Earth Science Froniters, 14(5): 133-146.

743 Gu, X. et al., 2010. The coupling relationship between metallization and hydrocarbon accumulation in
744 sedimentaty basins. Earth Science Frontiers, 17(2): 83-105.
745 Gu, X. et al., 2013. The genetic relationship between Carlin-type gold deposits and paleo-petroleum
746 reservoirs in SW Guizhou, China: Evidence from organic petrography. Earth Science Froniters,
747 20(1): 92-106.
748 Gu, X.X. et al., 2012. Hydrocarbon- and ore-bearing basinal fluids: A possible link between gold
749 mineralization and hydrocarbon accumulation in the Youjiang Basin, South China. Mineralium
750 Deposita, 47(6): 663-682.
751 Hao, F. et al., 2015. The fate of CO_2 derived from thermochemical sulfate reduction (TSR) and effect of
752 TSR on carbonate porosity and permeability, Sichuan Basin, China. Earth-Science Reviews,
753 141: 154-177.
754 Hausen, D.M., 2000. Characterizing the textural features of gold ores for optimizing gold extraction.
755 JOM, 52(4): 14-16.
756 Hnatyshin, D. et al., 2020. Understanding the microscale spatial distribution and mineralogical
757 residency of Re in pyrite: Examples from carbonate-hosted Zn-Pb ores and implications for
758 pyrite Re-Os geochronology. Chemical Geology, 533: 119427.
759 Hnatyshin, D., Creaser, R.A., Wilkinson, J.J., Gleeson, S.A., 2015. Re-Os dating of pyrite confirms an
760 early diagenetic onset and extended duration of mineralization in the Irish Zn-Pb ore field.
761 Geology, 43(2): 143-146.
762 Hofstra, A.H., Cline, J.S., 2000. Characteristics and models for Carlin-type gold deposits. Reviews in
763 Economic Geology, 13: 163-220.
764 Hu, R., Su, W., Bi, X., Li, Z., 1995. A possible evolution way of ore-formation hydrothermal fluid for the
765 Carlin-type gold deposit in the Yunnan-Guizhou-Guangxi triangle area. Acta Mineralogica
766 Sinica, 15(2): 144-149.
767 Hu, R.Z., Su, W.C., Bi, X.W., Tu, G.Z., Hofstra, A.H., 2002. Geology and geochemistry of Carlin-type gold
768 deposits in China. Mineralium Deposita, 37(3-4): 378-392.
769 Hu, S., He, L., Wang, J., 2000. Heat flow in the continental area of China: a new data set. Earth and
770 Planetary Science Letters, 179(2): 407-419.
771 Hulen, J.B., Collister, J.W., 1999. The oil-bearing, Carlin-type gold deposits of Yankee Basin, Alligator
772 Ridge district, Nevada. Economic Geology, 94(7): 1029-1049.
773 Hulen, J.B., Collister, J.W., Stout, B., Curtiss, D.K., Dahdah, N.F., 1998. The exhumed “Carlin-type” fossil
774 oil reservoir at Yankee Basin. JOM, 50(12): 30-34.
775 Jaireth, S., McKay, A., Lambert, I., 2008. Association of large sandstone uranium deposits with
776 hydrocarbons. AusGeo News, 89(6): 1-6.
777 Jin, X., 2017. Geology, mineralization and genesis of the Nibao, Shuiyindong and Yata gold deposits in
778 SW Guizhou Province, China, China University of Geoscience, Wuhan, 208 pp.
779 Jin, X. et al., 2016. Relationship between Carlin-type gold deposits and paleopetroleum reservoirs in
780 SW Guizhou, China: Evidence from gas compositions of fluid inclusions and Raman
781 spectroscopic characteristics of bitumen. Acta Petrologica Sinica, 32(11): 3295-3311.
782 Kelley, K.D., Selby, D., Falck, H., Slack, J.F., 2017. Re-Os systematics and age of pyrite associated with
783 stratiform Zn-Pb mineralization in the Howards Pass district, Yukon and Northwest Territories,
784 Canada. Mineralium Deposita, 52(3): 317-335.
785 Kendall, B., Creaser, R.A., Selby, D., 2009. ^{187}Re-^{187}Os geochronology of Precambrian organic-rich
786 sedimentary rocks. Geological Society of London, Special Publications, 326(1): 85-107.

787 Kesler, S.E. et al., 1994. Role of crude oil in the genesis of Mississippi Valley-type deposits: Evidence
788 from the Cincinnati arch. Geology, 22(7): 609-612.
789 Kribek, B., Zak, K., Spangenberg, J.E., Jehlicka, J., Kominek, J., 1999. Bitumens in the late Variscan
790 hydrothermal vein-type uranium deposit of Pribram, Czech Republic: Sources,
791 radiation-induced alteration, and relation to mineralization. Economic Geology, 94(7):
792 1093-1114.
793 Lai, C.-K. et al., 2014. The western Ailaoshan volcanic belts and their SE Asia connection: A new
794 tectonic model for the Eastern Indochina Block. Gondwana Research, 26(1): 52-74.
795 Large, R.R., Bull, S.W., Maslennikov, V.V., 2011. A carbonaceous sedimentary source-rock model for
796 Carlin-type and orogenic gold deposits. Economic Geology, 106(3): 331-358.
797 Large, S.J.E. et al., 2016. Trace elements in fluid inclusions of sediment-hosted gold deposits indicate a
798 magmatic-hydrothermal origin of the Carlin ore trend. Geology, 44(12): 1015-1018.
799 Lawley, C., Selby, D., Imber, J., 2013. Re-Os molybdenite, pyrite, and chalcopyrite geochronology, Lupa
800 Goldfield, southwestern Tanzania: Tracing metallogenic time scales at midcrustal shear zones
801 hosting orogenic Au deposits. Economic Geology, 108(7): 1591-1613.
802 Lewan, M., 1985. Evaluation of petroleum generation by hydrous pyrolysis experimentation.
803 Philosophical Transactions of the Royal Society of London. Series A, Mathematical and
804 Physical Sciences, 315(1531): 123-134.
805 Li, Z. et al., 2017. Rhenium-osmium geochronology in dating petroleum systems: progress and
806 chanllenges. Acta Petrolei Sinica, 38(3): 297-306.
807 Lillis, P.G., Selby, D., 2013. Evaluation of the rhenium–osmium geochronometer in the Phosphoria
808 petroleum system, Bighorn Basin of Wyoming and Montana, USA. Geochimica et
809 Cosmochimica Acta, 118: 312-330.
810 Liu, J., Selby, D., 2017. A matrix matched reference material for validating petroleum Re-Os
811 measurements. Geostandards and Geoanalytical Research., 42(1): 97-113.
812 Liu, J., Selby, D., Obermajer, M., Mort, A., 2018. Re-Os geochronology and oil-source correlation of
813 Duvernay petroleum system, western Canada sedimentary basin: Implications for the
814 application of the Re-Os geochronometer to petroleum systems. AAPG Bulletin, 108(8):
815 1627-1657.
816 Liu, J., Ye, J., Liu, J., Jun, T., Niu, J., 2000. Oil accumulation and ore formation. Bulletin of Mineralogy
817 Petrology and Geochemistry, 19(3): 164-171.
818 Liu, T., Liu, B., Chen, G., Wu, Z., 2001. Tectonic evolution and hydrocarbon preservation region dividion
819 in Nanpanjiang Basin. Natural Gas Industry, 21(1): 18-23.
820 Liu, Y., Hu, K., Han, S., Sun, Z., 2016. The characteristics of organic matter and its relationship with the
821 formation of Carlin-type gold deposits in southwest Guizhou Province. Geochimica, 45(3):
822 281-302.
823 Ludwig, K., 2008. User's manual for Isoplot 3.7: A geochronological toolkit for Microsoft Excel:
824 Berkeley, California, Berkeley Geochronology Center, Special Publication No.4, 76 pp.
825 Machel, H.G., 2001. Bacterial and thermochemical sulfate reduction in diagenetic settings - Old and
826 new insights. Sedimentary Geology, 140(1–2): 143-175.
827 Machel, H.G., Krouse, H.R., Sassen, R., 1995. Products and distinguishing criteria of bacterial and
828 thermochemical sulfate reduction. Applied Geochemistry, 10(4): 373-389.

Mastalerz, M., Bustin, R.M., Sinclair, A.J., Stankiewicz, B.A., 1995. Carbon-rich material in the Erickson hydrothermal system, northern British Columbia, Canada; origin and formation mechanisms. Economic Geology, 90(4): 938-947.

Migdisov, A. et al., 2017. Hydrocarbons as ore fluids. Geochemical Perspectives Letters, 5: 47-52.

Mirasol-Robert, A. et al., 2017. Evidence and origin of different types of sedimentary organic matter from a Paleoproterozoic orogenic Au deposit. Precambrian Research, 299: 319-338.

Mossman, D.J., Nagy, B., Davis, D.W., 1993. Comparative Molecular, Elemental, and U-Pb Isotopic Composition of Stratiform and Dispersed-Globular Matter in the Paleoproterozoic Uraniferous Metasediments, Elliot Lake, Canada. Energy Sources, 15(2): 377-387.

Muntean, J.L., 2018a. The Carlin gold system: Applications to exploration in Nevada and beyond. In: Muntean, J.L. (Ed.), Diversity in Carlin-style gold deposits. Society of Economic Geologists Special Publications, v. 20, pp. 39-88.

Muntean, J.L., 2018b. Diversity of Carlin-style gold deposits. In: Muntean, J.L. (Ed.), Diversity in Carlin-style gold deposits. Society of Economic Geologists Special Publications, v. 20, pp. 1-5.

Muntean, J.L., Cline, J.S., Simon, A.C., Longo, A.A., 2011. Magmatic–hydrothermal origin of Nevada's Carlin-type gold deposits. Nature Geoscience, 4(2): 122-127.

Nakai, S.I. et al., 1993. Rb-Sr dating of sphalerites from Mississippi Valley-type (MVT) ore deposits. Geochimica et Cosmochimica Acta, 57(2): 417-427.

Nutt, C.J., Hofstra, A.H., 2003. Alligator Ridge district, east-central Nevada: Carlin-type gold mineralization at shallow depths. Economic Geology, 98(6): 1225-1241.

Pan, C., Yu, L., Liu, J., Fu, J., 2006. Chemical and carbon isotopic fractionations of gaseous hydrocarbons during abiogenic oxidation. Earth and Planetary Science Letters, 246(1): 70-89.

Parnell, J., 1994. Geofluids: Origin, migration and evolution of fluids in sedimentary basins:Geological Society of London, Special Publications, 78, 374 pp.

Parnell, J., McCready, A., 2000. Paragenesis of gold- and hydrocarbon-bearing fluids in gold deposits, Organic Matter and Mineralisation: Thermal Alteration, Hydrocarbon Generation and Role in Metallogenesis. Springer, pp. 38-52.

Pearcy, E.C., Burruss, R.C., 1993. Hydrocarbons and Gold Mineralization in the Hot-Spring Deposit at Cherry Hill, California. In: Parnell, J., Kucha, H., Landais, P. (Eds.), Bitumens in Ore Deposits. Springer Berlin Heidelberg, Berlin, Heidelberg, pp. 117-137.

Peters, K., Walters, C., Moldowan, J., 2005. The biomarker guide, biomarkers and isotopes in Petroleum exploration and Earth history: New York, 1-2. Cambridge University Press, 961 pp.

Peucker‐Ehrenbrink, B., Jahn, B.m., 2001. Rhenium‐osmium isotope systematics and platinum group element concentrations: Loess and the upper continental crust. Geochemistry, Geophysics, Geosystems, 2(10): 2001GC000172.

Pi, Q., Hu, R., Xiong, B., Li, Q., Zhong, R., 2017. In situ SIMS U-Pb dating of hydrothermal rutile: Reliable age for the Zhesang Carlin-type gold deposit in the golden triangle region, SW China. Mineralium Deposita, 52(8): 1179-1190.

Powell, T.G., Macqueen, R.W., 1984. Precipitation of Sulfide Ores and Organic Matter: Sulfate Reactions at Pine Point, Canada. Science, 224(4644): 63-6.

Qin, J., Wu, Y., Yan, Y., Zhu, Z., 1996. Hercynian-Indosinian sedimentary-tectonic evolution of the Nanpanjiang Basin. Acta Geologica Sinica, 70(2): 99-107.

Robb, L.J., Meyer, F.M., 1995. The Witwatersrand Basin, South Africa: Geological framework and mineralization processes. Ore Geology Reviews, 10(2): 67-94.

873 Saintilan, N.J., Selby, D., Creaser, R.A., Dewaele, S., 2018. Sulphide Re-Os geochronology links
874 orogenesis, salt and Cu-Co ores in the Central African Copperbelt. Scientific Reports, 8(1):
875 14946.
876 Saintilan, N.J. et al., 2019. Petroleum as source and carrier of metals in epigenetic sediment-hosted
877 mineralization. Science Reports, 9(1): 8283.
878 Seal, R.R., II, 2006. Sulfur Isotope Geochemistry of Sulfide Minerals. Reviews in Mineralogy and
879 Geochemistry, 61(1): 633-677.
880 Seifert, W., Moldowan, J., 1986. Use of biological markers in petroleum exploration. Methods in
881 Geochemistry and Geophysics, 24: 261-290.
882 Selby, D., Creaser, R.A., 2005. Direct radiometric dating of hydrocarbon deposits using
883 rhenium-osmium isotopes. Science, 308(5726): 1293-1295.
884 Selby, D., Creaser, R.A., Dewing, K., Fowler, M., 2005. Evaluation of bitumen as a ^{187}Re–^{187}Os
885 geochronometer for hydrocarbon maturation and migration: A test case from the Polaris MVT
886 deposit, Canada. Earth and Planetary Science Letters, 235(1): 1-15.
887 Selby, D., Kelley, K.D., Hitzman, M.W., Zieg, J., 2009. Re–Os sulfide (bornite, chalcopyrite, and pyrite)
888 systematics of the carbonate-hosted copper deposits at Ruby Creek, southern Brooks Range,
889 Alaska. Economic Geology, 104(3): 437-444.
890 Shi, C. et al., 2020. Hydrocarbon evolution of the over-mature Sinian Dengying reservoir of the
891 Neoproterozoic Sichuan Basin, China: Insights from Re–Os geochronology. Marine and
892 Petroleum Geology, 122: 104726.
893 Shirey, S.B., Walker, R.J., 1995. Carius tube digestion for low-blank rhenium-osmium analysis.
894 Analytical Chemistry, 67(13): 2136-2141.
895 Smoliar, M.I., Walker, R.J., Morgan, J.W., 1996. Re-Os ages of group IIA, IIIA, IVA, and IVB iron
896 meteorites. Science, 271(5252): 1099-1102.
897 Stein, H.J., Morgan, J.W., Anders, S., 2000. Re-Os dating of low-level highly radiogenic (LLHR) sulfides:
898 The Harnas gold deposit, douthwest Sweden, records continental-scale tectonic events.
899 Economic Geology, 95(8): 1657-1671.
900 Su, W. et al., 2018. Carlin-type gold deposits in the Dian-Qian-Gui “golden triangle” of southwest China.
901 In: Muntean, J.L. (Ed.), Diversity in Carlin-style gold deposits. Society of Economic Geologists
902 Special Publications, v. 20, pp. 157-185.
903 Su, W., Hu, R., Xia, B., Xia, Y., Liu, Y., 2009. Calcite Sm-Nd isochron age of the Shuiyindong Carlin-type
904 gold deposit, Guizhou, China. Chemical Geology, 258(3): 269-274.
905 Su, W. et al., 2012. Mineralogy and geochemistry of gold-bearing arsenian pyrite from the Shuiyindong
906 Carlin-type gold deposit, Guizhou, China: Implications for gold depositional processes.
907 Mineralium Deposita, 47(6): 653-662.
908 Tan, Q.-P., Xia, Y., Xie, Z.-J., Yan, J., 2015. Migration paths and precipitation mechanisms of ore-forming
909 fluids at the Shuiyindong Carlin-type gold deposit, Guizhou, China. Ore Geology Reviews, 69:
910 140-156.
911 Thomson, M.L., Mastalerz, M., Sinclair, A.J., Bustin, R.M., 1992. Fluid source and thermal history of an
912 epithermal vein deposit, Owen Lake, central British Columbia: evidence from bitumen and
913 fluid inclusions. Mineralium Deposita, 27(3): 219-225.
914 Völkening, J., Walczyk, T., Heumann, K.G., 1991. Osmium isotope ratio determinations by negative
915 thermal ionization mass spectrometry. International Journal of Mass Spectrometry and Ion
916 Processes, 105(2): 147-159.

Wang, G., 1992. Three stronitum and rubidium isotime ages in northwest Guangxi. Geology of Guangxi, 5(1): 29-35.

Wells, J.D., Mullens, T.E., 1973. Gold-bearing arsenian pyrite determined by microprobe analysis, Cortez and Carlin gold mines, Nevada. Economic Geology, 68(2): 187-201.

Williams-Jones, A.E., Bowell, R.J., Migdisov, A.A., 2009. Gold in Solution. Elements, 5(5): 281-287.

Wilson, N.S.F., Zentilli, M., 2006. Association of pyrobitumen with copper mineralization from the Uchumi and Talcuna districts, central Chile. International Journal of Coal Geology, 65(1): 158-169.

Worden, R.H., Smalley, P.C., 1996. H_2S-producing reactions in deep carbonate gas reservoirs: Khuff Formation, Abu Dhabi. Chemical Geology, 133(1): 157-171.

Wu, C., 2012. Organic matter in Carlin-type gold deposits and paleo-oil reservoirs in southwest Guizhou - Source, maturity and association, China University of Geosciences, Beijing, 91 pp.

Wu, Y.-F. et al., 2020. Distribution of trace elements between carbonaceous matter and sulfides in a sediment-hosted orogenic gold system. Geochimica et Cosmochimica Acta, 276: 345-362.

Xie, Z. et al., 2018a. Are there Carlin-type gold deposits in China? A comparison of the Guizhou, China, deposits with Nevada, USA, deposits. In: Muntean, J.L. (Ed.), Diversity in Carlin-style gold deposits. Society of Economic Geologists Special Publications, v. 20, pp. 187-233.

Xie, Z. et al., 2018b. Magmatic Origin for Sediment-Hosted Au Deposits, Guizhou Province, China: In Situ Chemistry and Sulfur Isotope Composition of Pyrites, Shuiyindong and Jinfeng Deposits. Economic Geology, 113(7): 1627-1652.

Xiong, S.-F. et al., 2019. Gold distribution and source of the J4 gold-bearing breccia pipe in the Qiyugou district, North China Craton: Constraints from ore mineralogy and in situ analysis of trace elements and S-Pb isotopes. Ore Geology Reviews, 105: 514-536.

Yan, J. et al., 2018. NanoSIMS element mapping and sulfur isotope analysis of Au-bearing pyrite from Lannigou Carlin-type Au deposit in SW China: New insights into the origin and evolution of Au-bearing fluids. Ore Geology Reviews, 92: 29-41.

Zaw, K. et al., 2014. Tectonics and metallogeny of mainland Southeast Asia — A review and contribution. Gondwana Research, 26(1): 5-30.

Zhang, R.-X., Yang, S.-Y., 2016. A Mathematical Model for Determining Carbon Coating Thickness and Its Application in Electron Probe Microanalysis. Microscopy and Microanalysis, 22(6): 1374-1380.

Zhang, X.-C., Spiro, B., Halls, C., Stanley, C.J., Yang, K.-Y., 2003. Sediment-hosted disseminated gold deposits in southwest Guizhou, PRC: Their geological setting and origin in relation to mineralogical, fluid inclusion, and stable-isotope characteristics. International Geology Review, 45(5): 407-470.

Zhang, X., 1997. The geology and hydrothermal evolution of sediment-hosted gold deposits in Southwestern Guzhou Province, PRC: Unpublished Ph.D. Thesis, Imperial College of London, 273 pp.

Zhao, M., Zhang, S., Zhao, L., Liu, P., 2006a. Oil and gas accumulation and gas exploration potential in the Nanpanjiang Basin, China. Geological Review, 52(5): 642-649.

Zhao, M., Zhang, S., Zhao, L., Liu, P., 2006b. The thermal evolution history and oil and gas generation history of main source rocks in the Nanpanjiang Basin. Petroeum Geology & Experiment, 28(3): 271-275.

960 Zhao, M., Zhang, S., Zhao, L., Liu, P., Da, J., 2007. Geochemical characteristics and genesis of the
961 bitumen and gas in the Palaeo-reservoirs, Nanpanjiang Basin. Science in China Series D: Earth
962 Sciences, 37(2): 167-177.
963 Zhao, M., Zhao, L., Zhang, S., Liu, P., 2006c. Geochemical characteristics of main source rocks in the
964 Nanpanjiang Basin. Petroleum Geology & Experiment, 28(2): 162-167.
965 Zhou, M., 1999. A study on the pereoleum system of Nanpanjiang Sag. Yunnan Geology, 18(3):
966 248-265.
967 Zhu, G., Zhang, S., Liang, Y., Dai, J., Li, J., 2005. Isotope evidence for the TSR genesis high H2S natural
968 gas of the Feixianguan Formation, northeast Sichuan Basin. Science in China Series D: Earth
969 Sciences, 35(11): 1037-1046.
970 Zhu, G. et al., 2013. Alteration and multi-stage accumulation of oil and gas in the Ordovician of the
971 Tabei uplift, Tarim Basin, NW China: implications for genetic origin of the diverse
972 hydrocarbons. Marine and Petroleum Geology, 46: 234-250.
973 Zhu, J., Zhang, Z., Santosh, M., Jin, Z., 2020. Carlin-style gold province linked to the extinct Emeishan
974 plume. Earth and Planetary Science Letters, 530: 115940.
975 Zhuang, H., Lu, J., Fu, J., Liu, D., 2000. Organic petrological study on solid organic matter in two
976 Carlin-type gold deposits in the southwest Guizhou, China Scientia Geologica Sinica, 35(1):
977 83-90.
978 Zhuang, H., Lu, J., Fu, J., Ren, C., Zou, D., 1998. Crude oil as a carrier of gold migration: possible
979 petrological and geochemical evidence. Science in China Series D: Earth Sciences, 28(6):
980 552-558.
981 Zimmerman, A., Stein, H.J., Morgan, J.W., Markey, R.J., Watanabe, Y., 2014. Re–Os geochronology of
982 the El Salvador porphyry Cu–Mo deposit, Chile: Tracking analytical improvements in accuracy
983 and precision over the past decade. Geochimica et Cosmochimica Acta, 131: 13-32.

984

985

986

987 **Figure Captions**

988 Figure 1: Simplified geological map of Nanpanjiang Basin, South China block. (A)
989 Tectonic location map of Nanpanjiang Basin. (B) Simplified geological and structural
990 map of Nanpanjiang Basin, showing locations of both hydrocarbon reservoir and gold
991 deposits. F1: Mile-Shizong faults, F2: Ziyun-Du'an fault, F3: Napou-Funing fault, F4:
992 Pingxiang-Nanning fault, F5: Youjiang fault, F6: Poping thrust.

Figure 2: Comprehensive stratigraphic column of Nanpanjiang Basin showing hydrocarbon systems, gold deposits, and associated tectonic events.

Figure 3: Geological map of Laizishan–Yata–Banqi area showing sample locations of pyrobitumen and pyrite analyzed in this study.

Figure 4: Typical outcrop, reflected light images and BSE images of pyrobitumen and pyrite samples from Laizishan (LZS) and Banqi (BQ) reservoirs, and Yata (YT) gold deposit analyzed in this study. (a) Pyrobitumen associating with calcite from the Permian Wujiaping Formation, Laizishan reservoir. (b) Typical reflected light images of the calcite, pyrobitumen and pyrite in the Laizishan reservoir with pyrobitumen and pyrite together present in pore spaces between calcite grains. (c) Pyrobitumen and associated calcite in the Permian Wujiaping Limestome, Banqi reservoir. (d) Typical reflected light images in the Banqi reservoir showing pyrobitumen and pyrite together distributed along the boundary of calcite grains. (e) Disseminated pyrite hosted in siltstone of the Middle Triassic Xinyuan Formation, Yata deposit. (f) Typical reflected light images showing shape and distribution of pyrite grains in the Yata deposit. (g) backscattered electron (BSE) image showing the feature of pyrite grains (YT-31) in the Yata deposit. (h) backscattered electron (BSE) image showing the rim-core structure of the pyrite (YT-43) with rim contains higher Au than the core. The yellow points in g and h are the EPMA locations. Mineral abbreviations: Py – pyrite, Cal – calcite, Bt – pyrobitumen

Figure 5: Traditional $^{187}Re/^{188}Os$ vs. $^{187}Os/^{188}Os$ plot showing all Re-Os pyrobitumen data from Laizishan and Banqi reservoirs. Data labels are sample numbers listed in Table 1. MSWD = mean square weighted deviation. See text for discussion.

Figure 6: Traditional $^{187}Re/^{188}Os$ vs. $^{187}Os/^{188}Os$ plot showing Re-Os data for all pyrite samples from Yata (YT) gold deposit. Data labels are sample numbers listed in Table 2. MSWD = mean square weighted deviation. See text for discussion.

Figure 7: Basin modeling of strata in Yang-1 well in Nanpanjiang Basin, showing key interval of petroleum evolution (modified from Zhao et al., 2006).

Figure 8: Compiled chronology and mineral formation sequence in Nanpanjiang Basin. Cited references are (1) Hu et al., 1995; (2) Jin, 2017; (3) Wang, 1992; (4) Chen et al.,2015; (5) Pi et al., 2017; (6) Chen et al., 2009; (7) Gu et al., 2012; (8) Su et al., 2009.

Figure 9: Simplified model for relationship between hydrocarbon evolution and Carlin-type gold deposits in Nanpanjiang Basin

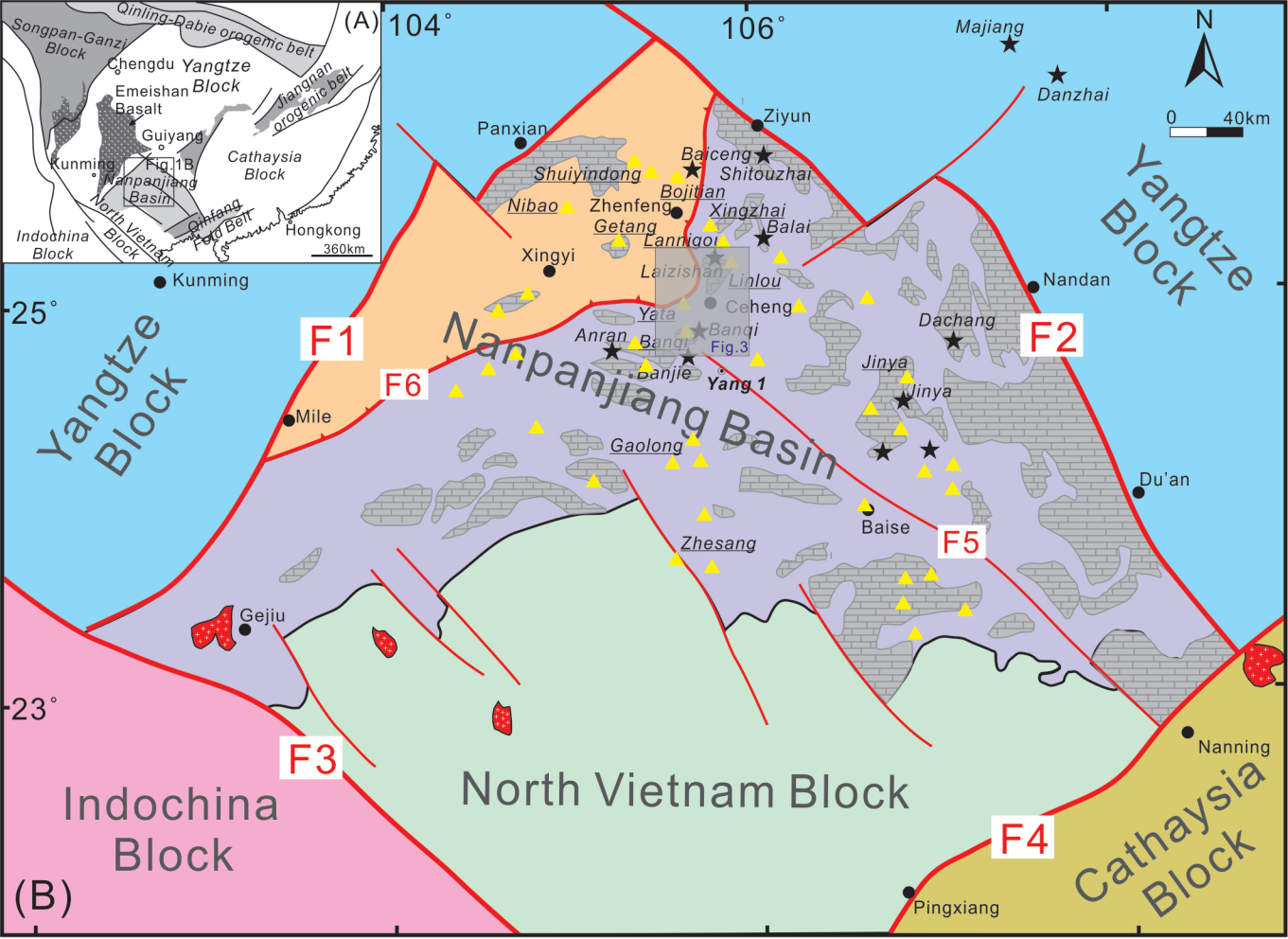
(A)
Songpan-Ganzi Block
Qinling-Dabie orogenic belt
Chengdu
Yangtze Block
Emeishan Basalt
Jiangnan orogenic belt
Guiyang
Kunming
Fig.1B
Cathaysia Block
Nanpanjiang Basin
North Vietnam Block
Qinfang Fold Belt
Hongkong
360km
Indochina Block
Kunming
104°
106°
25°
23°
N
0 40km
Majiang
Danzhai
Ziyun
Panxian
Baiceng
Shitouzhai
Shuiyindong
Bojitan
Nibao
Zhenfeng
Xingzhai
Balai
Getang
Lannigou
Xingyi
Laizishan
Linlou
Ceheng
Nandan
Yata
Anran
Bangqi
Fig.3
Dachang
Jinya
Banjie
Yang 1
Jinya
F1
F2
F6
Nanpanjiang Basin
Yangtze Block
Yangtze Block
Mile
Gaolong
Du'an
Baise
F5
Zhesang
Gejiu
Nanning
F3
Indochina Block
North Vietnam Block
F4
Cathaysia Block
(B)
Pingxiang
Indochina Block
Yangtze Block
Cathaysia Block
North Vietnam Block
Platform facies
Basin facies
Carbonate platform
Granite
Fault
Gold deposit
Paleo-reservoirs
City
Well

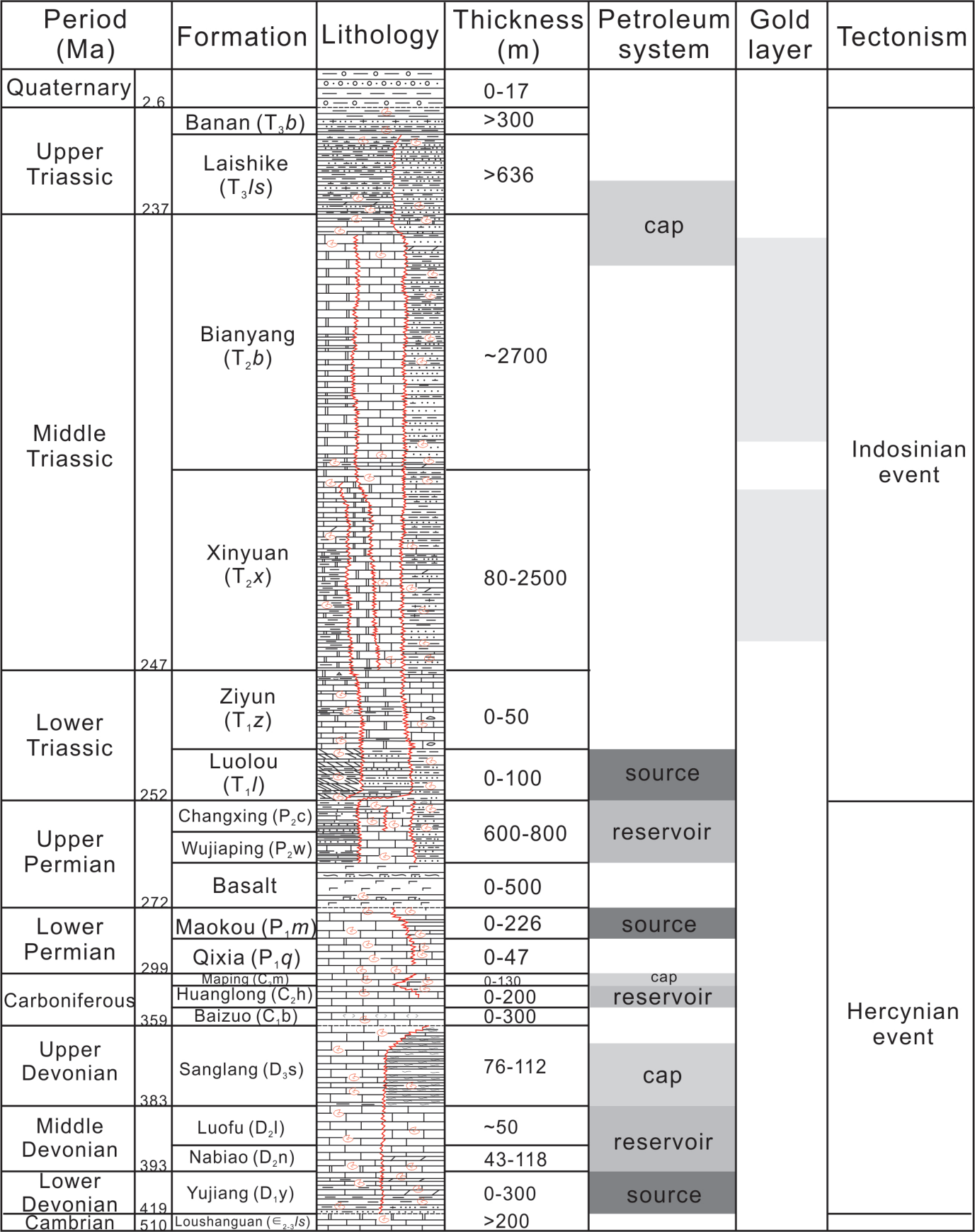
Period (Ma)
Formation
Lithology
Thickness (m)
Petroleum system
Gold layer
Tectonism
Quaternary
2.6
0-17
Upper Triassic
Banan (T_3b)
>300
Laishike (T_3ls)
>636
237
cap
Middle Triassic
Bianyang (T_2b)
~2700
Xinyuan (T_2x)
80-2500
247
Indosinian event
Lower Triassic
Ziyun (T_1z)
0-50
Luolou (T_1l)
0-100
source
252
Upper Permian
Changxing (P_2c)
Wujiaping (P_2w)
600-800
reservoir
Basalt
0-500
272
Lower Permian
Maokou (P_1m)
0-226
source
Qixia (P_1q)
0-47
299
Maping (C_2m)
0-130
cap
Carboniferous
Huanglong (C_2h)
0-200
reservoir
Baizuo (C_1b)
0-300
359
Upper Devonian
Sanglang (D_3s)
76-112
cap
383
Middle Devonian
Luofu (D_2l)
~50
reservoir
Nabiao (D_2n)
43-118
393
Lower Devonian
Yujiang (D_1y)
0-300
source
419
Hercynian event
Cambrian
510
Loushanguan ($\in_{2-3}ls$)
>200

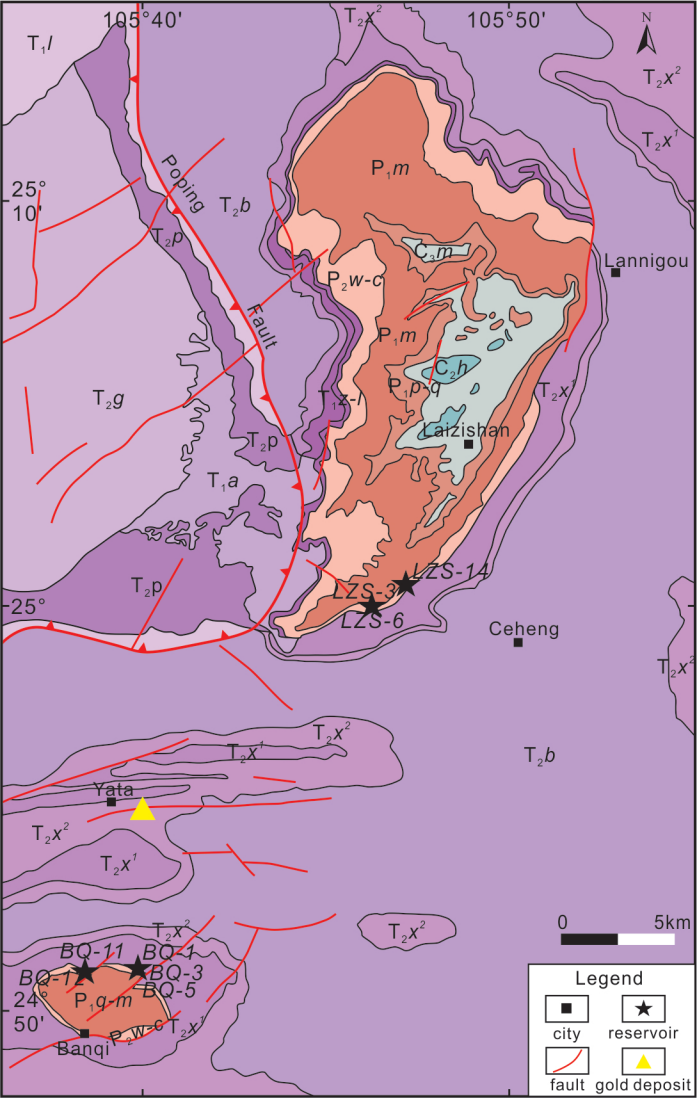
105°40'
105°50'
N
25° 10'
25°
24° 50'
Poping Fault
Lannigou
Laizishan
Ceheng
Yata
Banqi
LZS-11
LZS-3
LZS-6
BQ-11
BQ-1
BQ-12
BQ-3
BQ-5
T_1l
T_2x^2
T_2x^1
T_2b
T_2p
P_1m
C_2m
P_2w-c
C_2h
P_1p-q
T_2z-l
T_2g
T_1a
P_1q-m
P_2w-c
0
5km
Legend
city
reservoir
fault
gold deposit

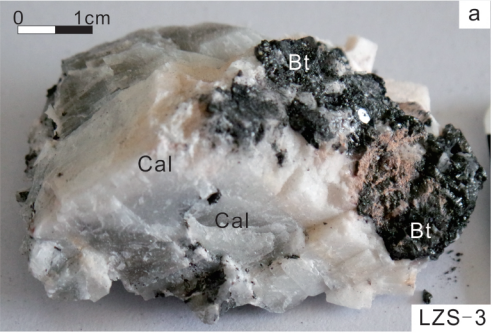
0 1cm
a
Bt
Cal
Cal
Bt
LZS-3

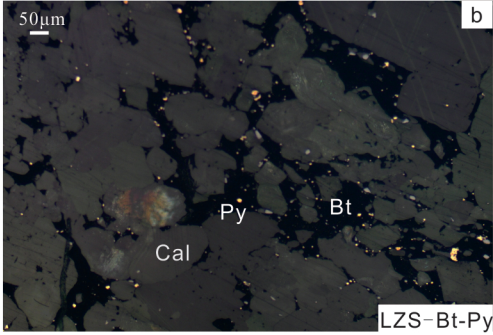
50μm
b
Py
Bt
Cal
LZS-Bt-Py

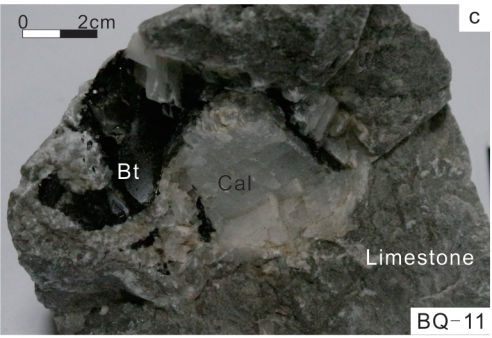
0 2cm
c
Bt
Cal
Limestone
BQ-11

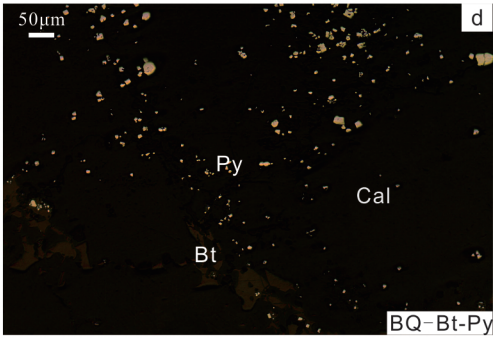
50μm
d
Py
Cal
Bt
BQ-Bt-Py

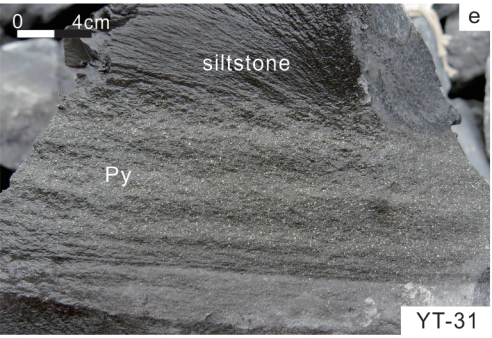
0 4cm
e
siltstone
Py
YT-31

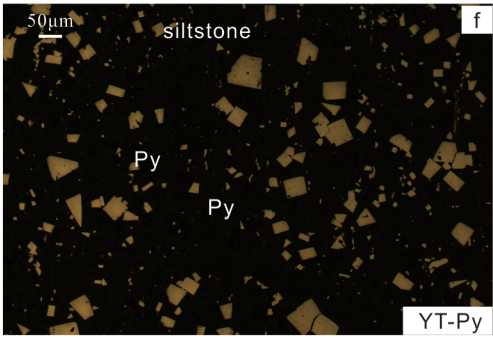
50μm
siltstone
f
Py
Py
YT-Py

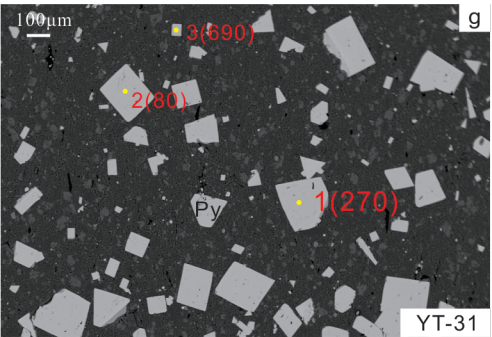
100μm
g
3(690)
2(80)
Py
1(270)
YT-31

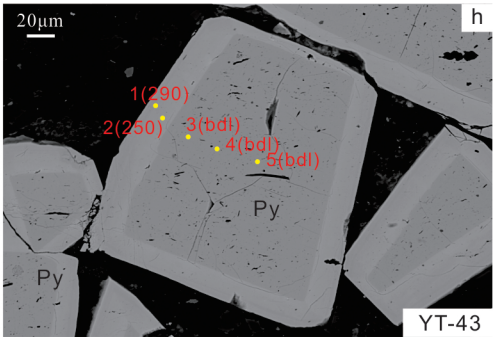
20μm
h
1(290)
2(250)
3(bdl)
4(bdl)
5(bdl)
Py
Py
YT-43

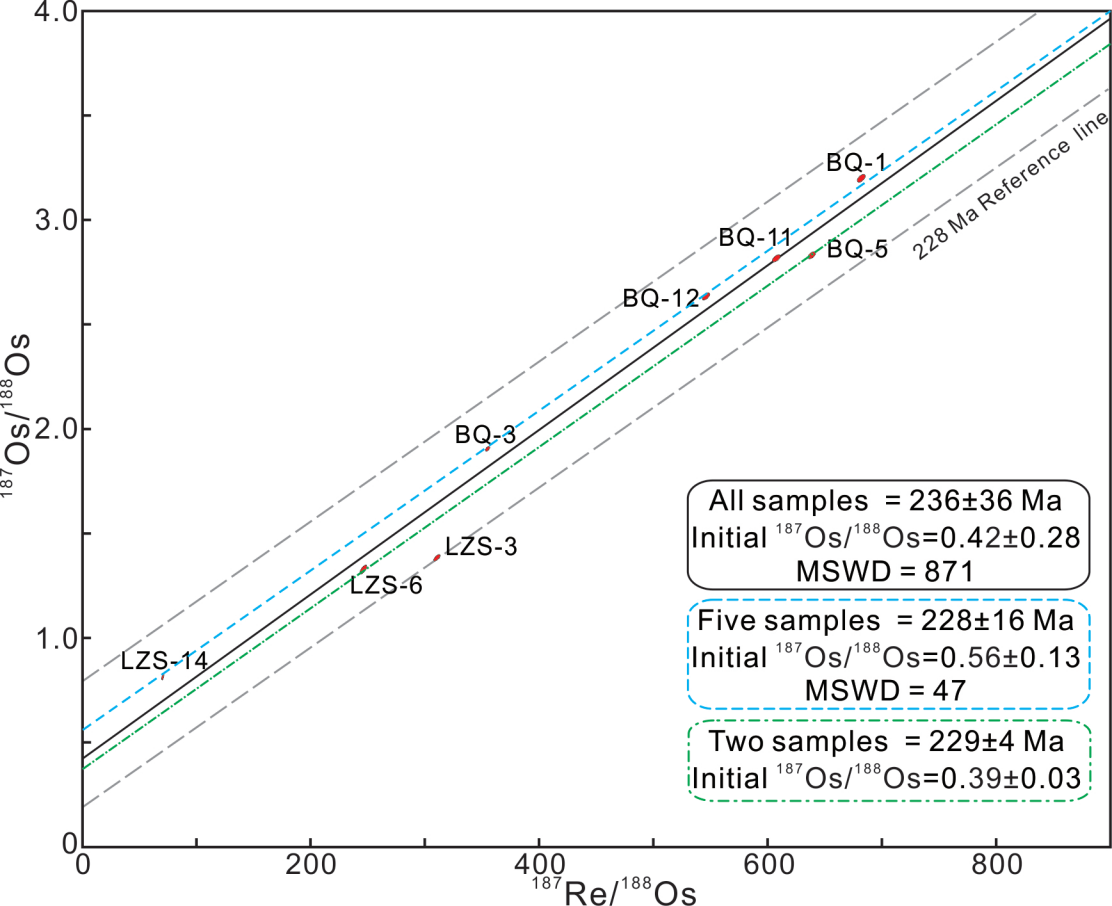
4.0
3.0
2.0
1.0
0
0
200
400
600
800
$^{187}Os/^{188}Os$
$^{187}Re/^{188}Os$
BQ-1
BQ-11
BQ-5
BQ-12
BQ-3
LZS-3
LZS-6
LZS-14
228 Ma Reference line
All samples = 236±36 Ma
Initial $^{187}Os/^{188}Os$=0.42±0.28
MSWD = 871
Five samples = 228±16 Ma
Initial $^{187}Os/^{188}Os$=0.56±0.13
MSWD = 47
Two samples = 229±4 Ma
Initial $^{187}Os/^{188}Os$=0.39±0.03

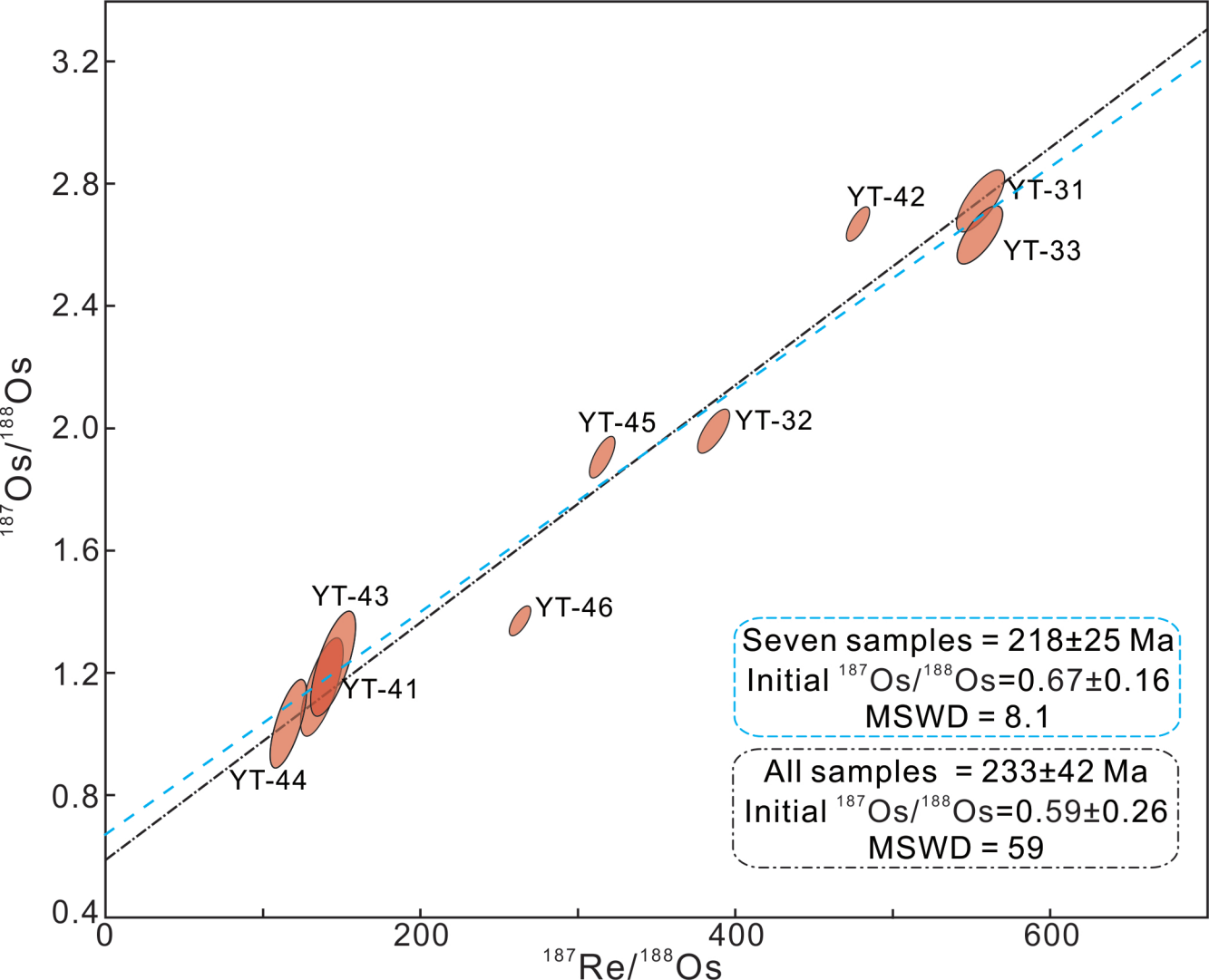
3.2
2.8
2.4
2.0
1.6
1.2
0.8
0.4
0
200
400
600
$^{187}Os/^{188}Os$
$^{187}Re/^{188}Os$
YT-42
YT-31
YT-33
YT-45
YT-32
YT-43
YT-46
YT-41
YT-44
Seven samples = 218±25 Ma
Initial $^{187}Os/^{188}Os$=0.67±0.16
MSWD = 8.1
All samples = 233±42 Ma
Initial $^{187}Os/^{188}Os$=0.59±0.26
MSWD = 59

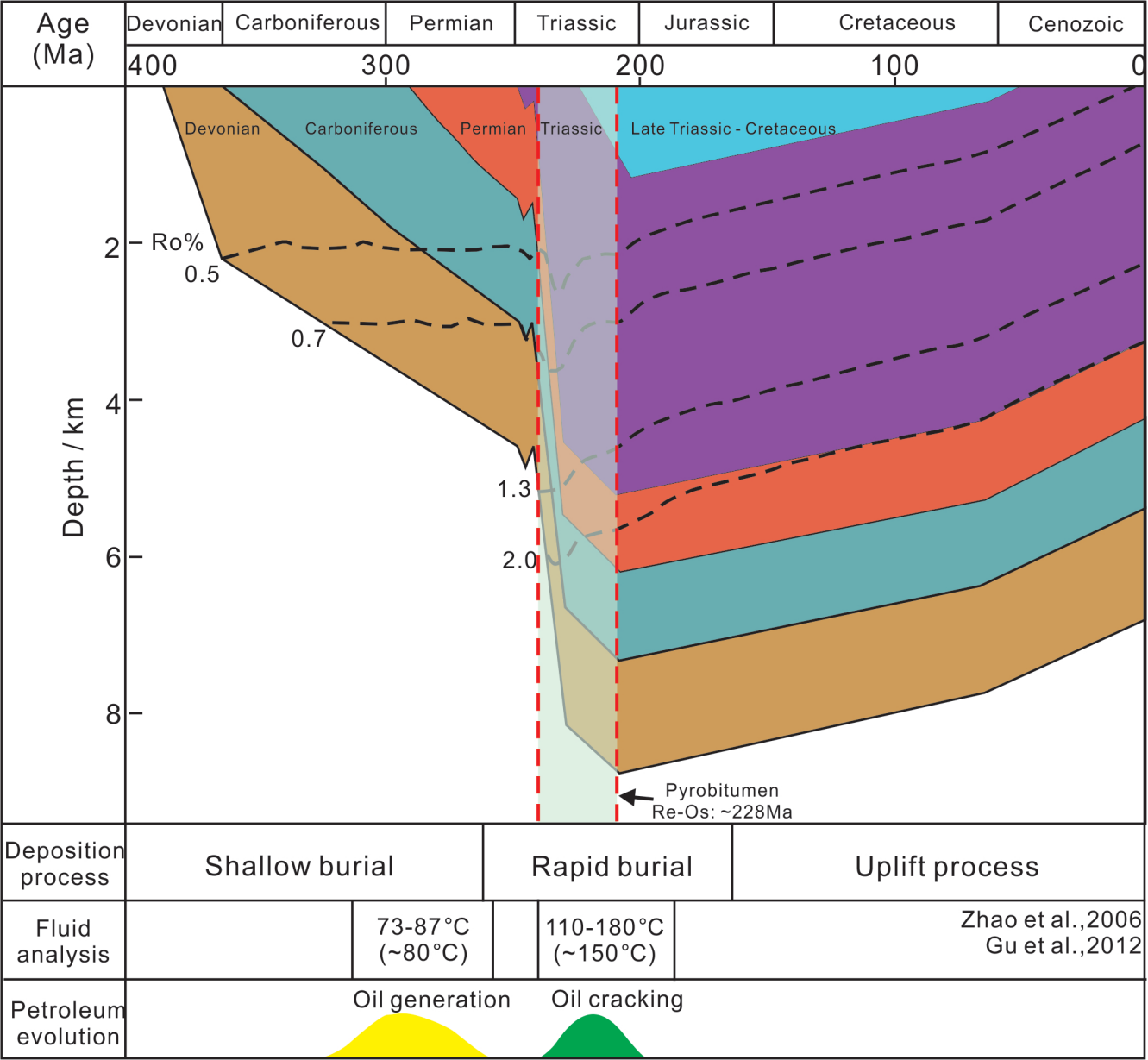
Age (Ma)
Devonian
Carboniferous
Permian
Triassic
Jurassic
Cretaceous
Cenozoic
400
300
200
100
0
Devonian
Carboniferous
Permian
Triassic
Late Triassic - Cretaceous
Ro%
0.5
0.7
1.3
2.0
Depth / km
2
4
6
8
Pyrobitumen
Re-Os: ~228Ma
Deposition process
Shallow burial
Rapid burial
Uplift process
Fluid analysis
73-87°C
(~80°C)
110-180°C
(~150°C)
Zhao et al.,2006
Gu et al.,2012
Petroleum evolution
Oil generation
Oil cracking

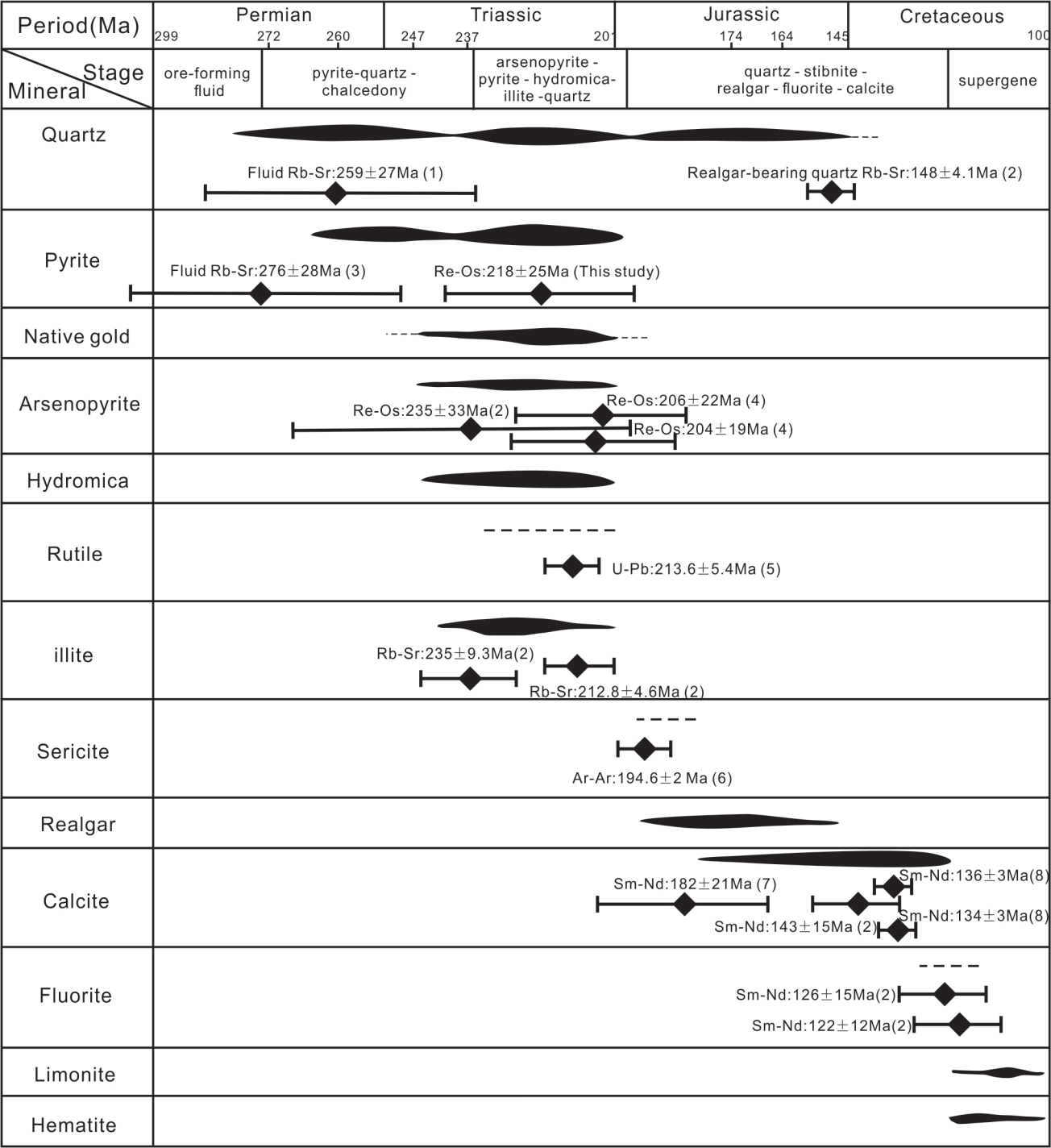
Period(Ma)
Permian
Triassic
Jurassic
Cretaceous
299
272
260
247
237
201
174
164
145
100
Stage
Mineral
ore-forming fluid
pyrite-quartz - chalcedony
arsenopyrite - pyrite - hydromica- illite -quartz
quartz - stibnite - realgar - fluorite - calcite
supergene
Quartz
Fluid Rb-Sr:259±27Ma (1)
Realgar-bearing quartz Rb-Sr:148±4.1Ma (2)
Pyrite
Fluid Rb-Sr:276±28Ma (3)
Re-Os:218±25Ma (This study)
Native gold
Arsenopyrite
Re-Os:235±33Ma(2)
Re-Os:206±22Ma (4)
Re-Os:204±19Ma (4)
Hydromica
Rutile
U-Pb:213.6±5.4Ma (5)
illite
Rb-Sr:235±9.3Ma(2)
Rb-Sr:212.8±4.6Ma (2)
Sericite
Ar-Ar:194.6±2 Ma (6)
Realgar
Calcite
Sm-Nd:182±21Ma (7)
Sm-Nd:136±3Ma(8)
Sm-Nd:143±15Ma (2)
Sm-Nd:134±3Ma(8)
Fluorite
Sm-Nd:126±15Ma(2)
Sm-Nd:122±12Ma(2)
Limonite
Hematite

Event	Time	Temperaure	Model
Gold-bearing pyrite formation	Late Triassic (~218Ma)	184-228 ºC	
Gas and pyrobitumen formation	Late Triassic (~228Ma)	110-180 ºC	
Oil formation	Carboniferous - Triassic	73-87 ºC	

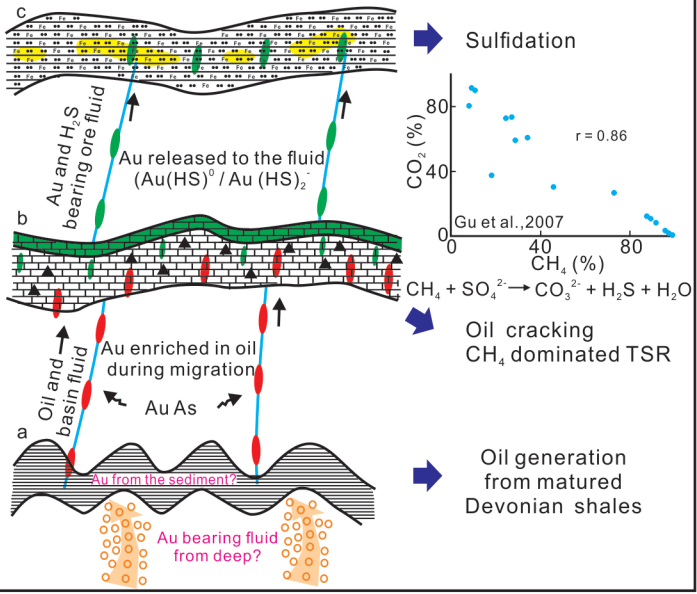

shale | limestone | siltstone | oil | gas | bitumen | deep fluid | basin fluid | gold deposit

Table 1. Rhenium–Osmium Elemental and Isotopic Data for Bitumen from Banqi and Laizishan reservoir, Nanpanjiang Basin

Sample	Latitude	Longitude	Formation	Re (ppb)	±	Os (ppt)	±	^{192}Os (ppt)	±	^{187}Os (ppt)	±	^{187}Re/^{188}Os	±	^{187}Os/^{188}Os	±	rho	Osi $_{236}$	±
BQ-1	24°51’35’’	105°40’21’’	Wujiaping	238.6	0.60	2360.6	12.7	695.1	2.4	704.8	2.4	683.0	2.9	3.209	0.015	0.571	0.52	0.03
BQ-3	24°51’35’’	105°40’21’’	Wujiaping	48.4	0.12	810.5	3.8	271.6	1.0	163.7	0.6	354.4	1.6	1.907	0.010	0.586	0.51	0.02
BQ-5	24°51’35’’	105°40’21’’	Wujiaping	175.4	0.44	1789.7	9.3	545.7	1.9	489.8	1.7	639.6	2.7	2.841	0.014	0.576	0.32	0.02
BQ-11	24°50’57’’	105°39’11’’	Wujiaping	101.4	0.26	1085.4	5.7	331.4	1.2	295.9	1.0	608.4	2.7	2.826	0.014	0.593	0.43	0.02
BQ-12	24°50’57’’	105°39’11’’	Wujiaping	140.7	0.38	1647	8.8	511.9	2.0	427.6	1.6	546.8	2.6	2.644	0.014	0.612	0.49	0.02
LZS-3	24°59’59’’	105°46’29’’	Wujiaping	11.6	0.03	209.2	1.3	74.2	0.5	32.5	0.2	309.9	2.3	1.386	0.013	0.702	0.17	0.02
LZS-6	24°59’59’’	105°46’29’’	Wujiaping	12.1	0.04	273.7	2.0	97.7	1.0	41.0	0.4	245.5	2.5	1.330	0.018	0.702	0.36	0.03
LZS-14	25°0’33’’	105°47’0’’	Wujiaping	5.2	0.02	405.5	2.5	153.5	1.4	40.0	0.4	67.6	0.7	0.824	0.010	0.642	0.56	0.01

Table 2. Rhenium–Osmium Elemental and Isotopic Data for pyrite from Yata gold deposit, Nanpanjiang Basin

Sample	Latitude	Longitude	Formation	Re (ppb)	±	Os (ppt)	±	^{192}Os (ppt)	±	^{187}Re/^{188}Os	±	^{187}Os/^{188}Os	±	rho	Osi_{233}	±
YT-31	24°54'59''	105°39'13''	Xinyuan	3.26	0.01	37.9	0.6	11.6	0.3	556.5	12.5	2.75	0.08	0.729	0.59	0.13
YT-32	24°54'59''	105°39'13''	Xinyuan	3.19	0.01	49.5	0.7	16.4	0.4	386.5	8.3	2.00	0.06	0.717	0.49	0.09
YT-33	24°54'59''	105°39'13''	Xinyuan	4.67	0.01	53.7	0.8	16.7	0.4	556.3	11.9	2.64	0.08	0.717	0.48	0.12
YT-41	24°55'01''	105°39'12''	Xinyuan	1.16	0.01	46.2	1.7	16.8	1.4	136.8	11.1	1.16	0.13	0.708	0.62	0.17
YT-42	24°55'01''	105°39'12''	Xinyuan	7.89	0.02	105.8	1.1	32.8	0.4	478.7	6.0	2.68	0.05	0.703	0.81	0.07
YT-43	24°55'01''	105°39'12''	Xinyuan	1.12	0.01	43.1	1.6	15.5	1.3	144.0	11.7	1.23	0.14	0.708	0.67	0.19
YT-44	24°55'01''	105°39'12''	Xinyuan	0.63	0.01	29.6	1.1	10.9	0.9	115.5	9.4	1.04	0.12	0.708	0.59	0.15
YT-45	24°55'01''	105°39'12''	Xinyuan	3.53	0.01	66.6	0.9	22.3	0.5	315.1	6.6	1.91	0.06	0.710	0.68	0.08
YT-46	24°55'01''	105°39'12''	Xinyuan	3.94	0.02	84.0	1.1	29.8	0.6	262.8	5.6	1.37	0.04	0.693	0.35	0.06

Table 3. Electron Microprobe Analysis of gold bearing from the Yata deposit

Sample No.	mineral	Au (wt%)	As (wt%)	Fe (wt%)	S (wt%)	Ag (wt%)	Sb (wt%)	Zn (wt%)	Cu (wt%)	Total
YT-31	Pyrite	0.064	0.05	46.40	54.13	0.02	b.d.	b.d.	0.02	100.69
YT-31	Pyrite	0.030	0.06	46.39	54.14	b.d.	0.01	0.03	b.d.	100.67
YT-31	Pyrite	b.d.	0.08	46.09	53.67	0.01	b.d.	0.01	0.02	99.87
YT-31	Pyrite	b.d.	0.28	45.22	53.04	b.d.	b.d.	b.d.	0.01	98.55
YT-32	Pyrite	0.027	0.08	46.47	53.62	0.01	b.d.	b.d.	b.d.	100.20
YT-32	Pyrite	0.080	b.d.	46.48	53.61	0.01	b.d.	0.02	b.d.	100.19
YT-32	Pyrite	b.d.	0.20	46.22	53.50	b.d.	b.d.	b.d.	0.01	99.92
YT-32	Pyrite	0.069	b.d.	46.01	53.69	b.d.	b.d.	b.d.	b.d.	99.77
YT-41	Pyrite	0.050	0.04	46.02	53.03	b.d.	b.d.	b.d.	0.01	99.16
YT-41	Pyrite	b.d.	0.07	46.23	53.60	b.d.	b.d	b.d.	0.02	99.92
YT-41	Pyrite	0.024	2.38	45.76	51.05	b.d.	0.02	b.d.	0.01	99.25
YT-41	Pyrite	0.050	5.84	44.56	48.71	b.d.	0.01	b.d.	b.d.	99.18
YT-41	Pyrite	0.021	3.91	44.59	51.06	b.d.	b.d.	b.d.	b.d.	99.57
YT-41	Pyrite	0.038	0.17	46.03	53.48	0.01	b.d.	b.d.	b.d.	99.73
YT-42	Pyrite	0.033	0.10	46.08	53.12	b.d.	b.d.	b.d.	b.d.	99.33
YT-42	Pyrite	0.037	3.30	45.48	51.61	b.d.	b.d.	b.d.	b.d.	100.43
YT-42	Pyrite	b.d.	0.05	46.17	53.84	b.d.	b.d.	b.d.	0.03	100.07
YT-42	Pyrite	0.018	4.07	45.70	50.93	b.d.	b.d.	b.d.	0.01	100.73
YT-42	Pyrite	0.027	0.08	46.68	53.55	b.d.	0.01	0.01	b.d.	100.36
YT-42	Pyrite	0.013	0.07	46.80	53.50	b.d.	0.01	0.01	0.02	100.43
YT-43	Pyrite	0.077	b.d.	46.72	53.70	0.01	0.01	0.01	0.01	100.53
YT-43	Pyrite	0.029	4.40	45.30	50.95	b.d.	b.d.	b.d.	0.03	100.71
YT-43	Pyrite	0.025	5.38	44.86	50.09	b.d.	b.d.	b.d.	0.01	100.37
YT-43	Pyrite	b.d.	0.13	46.60	53.69	b.d.	b.d.	b.d.	0.01	100.43
YT-43	Pyrite	b.d.	0.05	46.28	53.53	0.01	b.d.	0.01	b.d.	99.88
YT-43	Pyrite	b.d.	0.07	46.35	53.56	b.d.	b.d.	b.d.	b.d.	99.98
YT-44	Pyrite	0.026	0.05	46.28	53.75	0.01	b.d.	0.01	b.d.	100.14
YT-44	Pyrite	b.d.	0.07	45.88	53.62	0.01	0.01	b.d.	0.03	99.61
YT-44	Pyrite	0.036	0.05	45.75	52.77	b.d.	b.d.	b.d.	b.d.	98.60
YT-44	Pyrite	0.010	0.23	45.80	53.65	0.02	b.d.	b.d.	0.01	99.72
YT-44	Pyrite	0.031	b.d.	45.15	53.47	b.d.	0.01	b.d.	b.d.	98.66
YT-45	Pyrite	0.019	0.12	45.99	52.72	0.01	0.01	b.d.	0.01	98.89
YT-45	Pyrite	0.012	0.18	45.57	52.36	b.d.	0.01	b.d.	0.03	98.17
YT-45	Pyrite	0.043	0.19	45.83	52.86	b.d.	b.d.	b.d.	0.02	98.95
YT-45	Pyrite	b.d.	0.21	45.88	53.55	0.01	0.02	0.01	0.01	99.69
YT-45	Pyrite	0.009	b.d.	46.03	53.37	b.d.	b.d.	b.d.	b.d.	99.44
YT-46	Pyrite	b.d.	b.d.	46.46	53.71	0.03	b.d.	b.d.	b.d.	100.20
YT-46	Pyrite	0.050	0.07	46.29	53.84	0.02	b.d.	b.d.	b.d.	100.26
YT-46	Pyrite	0.018	0.03	46.52	53.71	b.d.	b.d.	0.03	b.d.	100.31
YT-46	Pyrite	b.d.	0.05	46.51	53.89	b.d.	b.d.	b.d.	b.d.	100.45

b.d. = below detection